Journal Pre-proof

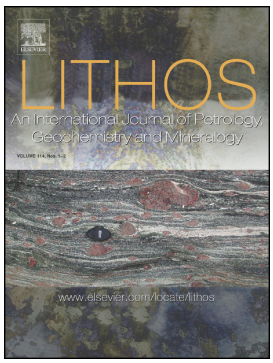

Co-occurrence of compositionally variable chromitites in the Sabzevar ophiolite, NE Iran

Alireza Eslami, Giovanni Grieco, Micol Bussolesi, Yuji Ichiyama, Davide Lenaz, Henrik Skogby, Anton V. Kutyrev, Alessandro Cavallo, Mohamed Zaki Khedr

PII: S0024-4937(23)00117-2

DOI: https://doi.org/10.1016/j.lithos.2023.107133

Reference: LITHOS 107133

To appear in: *LITHOS*

Received date: 29 October 2022

Revised date: 3 March 2023

Accepted date: 12 March 2023

Please cite this article as: A. Eslami, G. Grieco, M. Bussolesi, et al., Co-occurrence of compositionally variable chromitites in the Sabzevar ophiolite, NE Iran, *LITHOS* (2023), https://doi.org/10.1016/j.lithos.2023.107133

This is a PDF file of an article that has undergone enhancements after acceptance, such as the addition of a cover page and metadata, and formatting for readability, but it is not yet the definitive version of record. This version will undergo additional copyediting, typesetting and review before it is published in its final form, but we are providing this version to give early visibility of the article. Please note that, during the production process, errors may be discovered which could affect the content, and all legal disclaimers that apply to the journal pertain.

© 2023 Published by Elsevier B.V.

Journal Pre-proof

Co-occurrence of compositionally variable chromitites in the Sabzevar ophiolite, NE Iran

Alireza Eslami[1,2]*, Giovanni Grieco[3], Micol Bussolesi[4], Yuji Ichiyama[5], Davide Lenaz[6], Henrik Skogby[7], Anton V. Kutyrev[8], Alessandro Cavallo[4], Mohamed Zaki Khedr[9]

[1]M&U sas, 38360 Sassenage, France
[2]Université Grenoble Alpes, CNRS, ISTerre, F-38000 Grenoble, France
[3]Dipartimento di Scienze della Terra, Università degli Studi di Milano, via S. Botticelli, 23-20133 Milano, Italy
[4]University of Milan-Bicocca "Department of Earth and Environmental Sciences – DISAT, P.zza della Scienza 1–4, 2016 Milan, Italy
[5]Department of Earth Sciences, Chiba University, Chiba, Japan
[6]Department of Mathematics and Geosciences, University of Trieste, Via Weiss 8, 34128, Trieste, Italy
[7]Department of Geosciences, Swedish Museum of Natural History, Box 50007, 10405 Stockholm, Sweden
[8]Institute of Volcanology and Seismology, Far Eastern Branch of the Russian Academy of Sciences, Petropavlovsk-Kamchatsky, Russia
[9]Department of Geology, Faculty of Science, Kafrelsheikh University, Kafrelsheikh, Egypt

*Corresponding author: A. Eslami

E-mail address: alireza.eslami@univ-grenoble-alpes.fr

Journal Pre-proof

Abstract

The Sabzevar ophiolite belt consists of a series of thrust-bound massifs that widen in extent to ~150 km in NE Iran. The Kuh-Siah harzburgite-dunite massif in the central sector of this belt hosts abundant discontinuous pod-like chromitite deposits. These deposits are characterized by spinels with contrasting and variable compositions, but without any microtextural differences. The chromian spinel in these chromitite bodies displays a wide range of Cr-number (Cr/(Cr + Al)) atomic ratio from 0.50 to 0.77, and reveals a co-occurrence of Al-rich and Cr-rich chromitites within a single ophiolitic massif. Despite these chemical differences, primary spinels from both the high-Al and high-Cr chromitites have similar TiO_2 contents, indicating that they formed in a single tectono-magmatic setting. Both high-Al and high-Cr chromitite samples display low to moderate total platinum group element (PGE) abundances (85-537 ppb). Solid phases hosted by Cr-spinel grains in chromitites and their host dunites can be divided into three categories: platinum group minerals (PGM), base-metal minerals (BMM), and silicates. Euhedral quadrangular and round-shaped silicate inclusions consisting of clinopyroxene, orthopyroxene, Na-bearing phlogopite, serpentine and chlorite, are sporadically scattered in the Cr-spinel grains. These inclusions are mainly single crystals and rarely occur as polyphase assemblages. The BMM are mainly euhedral Ni- and Cu-rich sulfides with rare occurrence of pentlandite. The most widespread PGM are crystals of the laurite-erlichmanite series with subordinate malanite, braggite and BM-PGE-rich sulfides. Textural relationships reflect that the PGM are of magmatic origin. The BMM, on the other hand, formed during both magmatic and post-magmatic processes. The occurrence of low-temperature inclusions within Cr-spinel and ferrian Cr-spinel, comprising tremolite, chlorite and serpentine, are interpreted as post-magmatic entrapments of already-formed silicate phases at the time of grain boundary migration. Our petrographic observations and geochemical interpretations reveal that chromitites in the Kuh-Siah peridotite massif formed during multistage melt/fluid-peridotite reaction processes in an extended intra-oceanic arc–forearc setting located between the Turan and Central Iran continental blocks in the Mid to Late Cretaceous. Mössbauer measurements of $Fe^{3+}/\Sigma Fe$ ratios of Cr-spinels from the non-oxidized chromitite samples are relatively similar, more or less in the range 0.15-0.20, whereas those from the more oxidized chromitite samples have $Fe^{3+}/\Sigma Fe$ ratios in the range 0.28–0.62. Field observations and textural studies

Journal Pre-proof

suggest that the localized post-magmatic oxidation is linked to dominant hydrous fluids existing in the shear zone.

Journal Pre-proof

1. Introduction

Ophiolites are remnants of the oceanic lithosphere that have been tectonically emplaced onto continental margins (Dilek and Furnes, 2014). Harzburgitic mantle sections of ophiolite may host accumulation of spinel as podiform bodies, while the base of dunitic mantle-crust transition zone hosts stratiform ones (e.g. Ceuleneer and Nicolas, 1985; Augé, 1987; Lorand and Ceuleneer, 1989; Gauthier et al., 1990; Borisova et al., 2012; González-Jiménez et al., 2014; Khedr and Arai, 2016, 2017; Zaeimnia et al., 2017; Rospabé et al., 2019; Sepidbar et al., 2021; Moghadam et al., 2022). Accumulation of Cr-spinels in mantle peridotites leads to formation of varied textures comprising massive, semi-massive, disseminated, banded, and nodular types. Post-magmatic events, hydrothermal alteration, and/or metamorphism may alter the initial spinel composition leading to bimodality between high-Al and high-Cr end-members and/or continuity in spinel composition at different scales in ophiolitic rocks. Bimodality in spinel composition (high-Al and high-Cr) may occur in different peridotite massifs of the same ophiolite (e.g., Ahmed et al. 2001; Economou Eliopoulos, 1996; Uysal et al., 2009) or may coexist within a single peridotite massif (e.g., Leblanc, 1995; Melcher et al., 1997; Zaccarini et al., 2011; Khedr and Arai, 2016, 2017; Xiong et al., 2017b). Intermediate compositions between the two spinel end-members have also been recorded in ophiolitic chromitites (Uysal et al., 2016; Liu et al., 2019; Chen et al., 2019; Zhang et al., 2020; Bussolesi et al., 2022). All hypotheses for the co-occurrence of ophiolitic chromitites with variable composition have hitherto revolved around two processes: (i) continuous melting of upper mantle rocks which makes the residual peridotite assemblage different (e.g. Arai, 1992; Arai, 1994), so that, by increasing the degree of partial melting, the primary restite spinel becomes depleted in Al, Fe and Ti, while the Mg-number of both residual olivine and orthopyroxene increases (e.g. Jaques and Green, 1980; Michael and Bonatti, 1985; Zhou and Robinson, 1994); and (ii) crystallization of spinel from compositionally variable melts percolating through the mantle section and/or fluid-assisted processes of recrystallization (e.g. Ahmed and Arai, 2002; Uysal et al., 2009; Leblanc, 1995; Grahamet al., 1996; González-Jiménez et al., 2011; Derbyshire et al., 2013; Xiong et al., 2017a; Rollinson and Adetunji, 2015; Khedr and Arai, 2016, 2017; Uysal et al., 2018). Parental melts accountable for the formation of high-Al and high-Cr chromitites are thought to have MORB-like and boninitic compositions, respectively (Zhou et al., 1996, Zhou et al., 1998, Uysal et al., 2009; Khedr and Arai, 2016, 2017; Zaeimnia et al., 2017). However, detailed study of solid

inclusions and variations in fO_2 in compositionally variable chromitites is still poorly constrained.

Podiform chromitite bodies with very contrasting and continuous compositions are sporadically distributed in the mantle section of the Sabzevar ophiolite. Spinel in mantle peridotites from the Kuh-Siah massif in the Sabzevar ophiolite shows not only contrasting compositions as described before, but also a continuous range of compositions between high-Al and high-Cr end-members.

In this study, systematic field observations together with petrographic studies, geochemical fingerprints from Platinum Group Elements (PGE) bulk-analyses, electron microanalysis and oxygen fugacity aspects will be used to elucidate the nature of the processes that promoted compositionally heterogeneous chromitite formation in a segment of lithospheric mantle situated in the central sector of the northern Sabzevar ophiolitic belt. Although, Shafaii Moghadam et al. (2015) provided detailed mineralogical and geochemical study on the peridotites and associated chromitites from three chromitite deposits scattered in the Sabzevar ophiolite, our study focuses for the first time on the origin of PGM-bearing compositionally variable chromitites and the mantle oxidation state during their formation. This study also discusses the genesis and the genetic model for the formation of high-Al and high-Cr chromitites from a single peridotite massif based on solid inclusions within spinels and PGE bulk-analyses.

2. Geological setting

Mesozoic Neo-Tethyan ophiolitic massifs outcrop across different places in Iran, especially along the NE Iranian sector (Fig. 1a). A series of Upper Cretaceous ophiolite nappes are scattered along five alignments in NE Iran. These ophiolite assemblages include: 1) Northern Sabzevar ophiolite belt (NSOB); 2) Southern Sabzevar ophiolite belt (SSOB); 3) Bardeskan/Torbat-e-Hedarieh ophiolite slivers; 4) Fariman ophiolite mélange; and 5) Neyshabour ophiolite slices. These oceanic lithosphere fragments are bordered by two large-scale faults, the Dorouneh sinistral strike-slip fault in the south and the Sangbast–Shandiz dextral strike-slip fault to the north. The NSOB occurs as a continuous 150 km NW-SE trending belt, consisting of thrust-bound blocks of Neotethyan oceanic lithosphere (Fig. 1b). The study area belongs to the central sector of this belt. The central sector of NSOB is marked by two large km-scale peridotite massifs, namely Kuh-Siah and Olang-Sir (Fig. 1c). These massifs cover a rugged mountainous area of ~300 km^2 and are composed of the

following ophiolite lithologies (from top to bottom): (i) association of marine sediments, radiolarian cherts, pelagic limestones and pillow lavas; (ii) complex of sheeted dykes; (iii) layered, pegmatitic and isotropic gabbros; and (iv) a nappe of depleted mantle harzburgites with discordant dunite lenses. A dismembered tectonic sliver of mafic granulites embedded within the ophiolitic mélange is exposed to the south. Middle Eocene dacitic domes with adakite-like chemical characteristics are present to the south of these peridotite massifs. The major chromitite mining districts in the central sector of NSOB are situated in Kuh-Siah.

Most studies of these ophiolites have been focused on the NSOB (so-called "Sabzevar ophiolite"). Several hypotheses have been put forward to explain the geotectonic settings of the NSOB. Noghreyan (1982) suggested that the Sabzevar ophiolite was formed in a back-arc basin while Shojaat et al. (2003) argued that the Sabzevar ophiolite was emplaced during NE-dipping subduction of the northern branch of a narrow Tethyan ocean. In the same geodynamic context, Moghadam et al. (2014) argued the Sabzevar embryonic, subduction-related oceanic basin opened between the Lut Block to the south and the Turan block to the north since at least mid-Cretaceous. They also argued that intraoceanic subduction began before the Albian (100-113 Ma) and was responsible for generating magmas related to the suprasubduction zone (SSZ) within the Sabzevar oceanic lithosphere. Omrani et al. (2018) suggested that mafic rocks in these ophiolites formed in a SSZ setting within the Neotethys branch of the Sabzevar Ocean to the North of the Central Iranian Micro-continent (CIM). They also argued that there are similarities in ophiolite age, lithology and mineralization between NSOB and ophiolites in southern parts (SSOB and Bardeskan/Torbat-e-Heydarieyh) and that rotation or faulting of the CIM during Eocene resulted in detachment of the northern ophiolites from the southern ones (Omrani et al., 2018). The origin of the NSOB remains disputable with manifold and well-defended hypotheses.

The K-Ar geochronology of amphiboles from the lavas and diabases provided formation ages of 81.2 ± 4.1 Ma and 76.8 ± 3.8 Ma, respectively (Lensch and Davoudzadeh, 1982). Moghadam et al. (2014) reported zircon TIMS U–Pb dates of 100, 90 and 78 Ma for three plagiogranites and faunal dates of ~ 75–68 Ma for pelagic limestones between pillows lavas throughout the NSOB, indicating an extended period of formation of the ophiolitic sequences. The U-Pb ages from zircon (107.4 ± 2.4 Ma) and titanite (105.9 ± 2.3 Ma) in felsic segregation of mafic granulitic bodies in the central sector of NSOB have been interpreted to record peak metamorphism before the Late-Cretaceous Sabzevar back-arc basin development (Rossetti et al., 2010). It has also been argued that the formation of the Sabzevar migmatitic granulites was an upshot of the subduction of an early-formed Late Jurassic–Early Cretaceous

back-arc oceanic system, followed by extension of the Sabzevar back arc basin (Rossetti et al., 2010). A study of two chromitite varieties in three distinct peridotite massifs (i.e. Foroumad, Gaft, and Baghjar) throughout the NSOB (Moghadam et al., 2015) indicated that the formation of podiform chromitites can be ascribed to melt-rock reactions. It was also suggested that low-Cr chromitites initially formed via MORB-like melts during subduction initiation (an infant arc stage), whereas subsequent arc-like or boninitic melts were accountable for the high-Cr chromitites during a mature arc stage of the SSZ setting (Moghadam et al., 2015).

Several discontinuous chromitite bodies are enclosed as lenses or pods in a dunite envelope within harzburgite, in the Kuh-Siah massif in the central sector of the NSOB (Fig. 2). These chromitite deposits are spatially related to a single peridotite massif (Fig. 3a). The deposits possess a range of morphologies occurring either as elliptical to lenticular individual chromitite bodies (Fig. 3b) or as a series of discrete bodies (Fig. 3c). They are sub-discordant to concordant with the host harzburgite foliation. The orebodies range from a few centimeters to a few tens of meters in thickness. A variety of chromitite textures grading from low-grade disseminated to nodular and massive is observed in the studied chromitite deposits. The studied chromitite deposits are enveloped in dunites and are often offset and dismembered by oblique-slip faults. Most of the chromitite bodies were clustered along the NW-SE trending thrust fault system. A series of strike-slip faulting systems displaced different parts of the chromitite ore bodies. Determining and tracking these strike-slip faults is a traditional method to explore missing portions of chromitite bodies. Strong shearing deformation is seen in the examined ore bodies close to the thrust fault zone (Fig. 3d). These orebodies usually have a mylonitic structure.

3. Sampling and laboratory methods

Sampling localities were selected from nine outcrops, and twenty-three samples were examined under optical microscopes using both transmitted and reflected light.

Microanalyses of Cr-spinel and mineral inclusions in chromium spinel from twenty chromitite-dunite samples were performed with a JEOL8200 electron microprobe equipped with a wavelength dispersive system (SEM-WDS) at the University of Milan (Italy). The analytical conditions were 15 kV accelerating voltage, 15 nA beam current, 2 μm beam diameter, and 20 s counting time, using WDS detectors. Synthetic as well as natural standards

were used for calibration. It is crucial to note that only fresh cores of Cr-spinel and PGM inclusions suitable for in-situ microanalysis were taken into consideration. Quantitative chemical analyses of individual spinel in three harzburgite samples were collected using a JEOL JXA-8230 electron probe micro-analyzer (EPMA) equipped with five wavelength-dispersive spectrometers (WDS) and an energy-dispersive spectrometer (EDS) at the Institut des Sciences de la Terre, University Grenoble Alpes, France. Analyses were performed at 15 kV acceleration voltage, 100 nA beam current and a beam size with a diameter of ~ 1 μm. The concentrations of minor elements (Si, V, Ti, Ni, Co, Mn and Zn) and major elements (Fe, Cr, Al and Mg) of spinels were not only quantitatively measured by EPMA, but also the same minerals were qualitatively analysed by WDS and EDS. Total counting times (peak plus background) were 440 s for Si Kα; 240 s for V Kα, Ti Kα; 360 s for Co Kα; 180 s for Zn Kα; 100 s for Ni Kα and Mn Kα. Natural minerals, pure metals and synthetic oxides were used as standards and the ZAF correction was applied. Representative results of electron-microprobe analyses of Cr-spinels, silicate and sulfides inclusions are given in Table S1, Table S2 and Table S3, respectively.

The oxidation state of Fe in the studied samples was determined by Mössbauer spectroscopy at the Swedish Museum of Natural History in Stockholm using a conventional spectrometer system operated in constant acceleration mode. Small clean-looking Cr-spinel crystal fragments were hand-picked under the microscope from gently crushed sample parts (around cm-sized). To avoid other Fe-containing phases, the powdered samples were checked by powder X-ray diffraction (pXRD). Mössbauer absorbers were prepared by grinding 9 – 41 mg of sample material that was mixed with an acrylic resin and then pressed into 12-mm-diameter discs under mild heating. Spectra were collected at room temperature using a standard ^{57}Co source in a Rh matrix with a nominal activity of 50 mCi. Spectra were acquired over 1024 channels in the velocity range − 4.5 to + 4.5 mm/s and calibrated against an α-Fe foil before folding. The least-squares fitting software MossA 1.01f (Prescher et al. 2012) was applied to analyze the obtained spectra using a fitting model with one doublet assigned to Fe^{3+} and three doublets to Fe^{2+} (cf. Lenaz et al., 2018). Several studies have shown that the recoil-free fractions for Fe^{2+} and Fe^{3+} are unequal (e.g., De Grave and Van Alboom 1991; Eeckhout and De Grave 2003). Therefore, the absorption area ratios obtained for the Fe^{2+} and Fe^{3+} doublets were corrected for unequal recoil-free fractions based on the data presented in De Grave and Van Alboom (1991) and the composition of the studied samples, using recoilfree fractions of 0.687 for Fe^{2+} and 0.887 for Fe^{3+}.

Samples SI-2C and KE-2 showed anomalously high $Fe^{3+}/\Sigma Fe$ ratios that can be explained by ubiquitous ferrian Cr-spinel alteration, as shown by the SEM and EMPA studies. To avoid the ferrian Cr-spinel alteration, small pristine aliquots (< 1mg) were carefully selected and were run by use of a Mössbauer 10 mCi point-source. Representative examples of obtained spectra are shown in Fig. 4, and resulting Mössbauer parameters are given in Table S4.

Whole-rock PGE analyses were performed on twenty-one chromitite-dunite samples at two commercial laboratories. A first batch of chromitite-dunite samples from Ebrahim, Kalchenari1, Kalchenari-3, Kalchenari 5, Haj-Ghasem and Rohollah deposits was analyzed at the National Research Center of Geo-analysis, Chinese Academy of Sciences (CAS), by Inductively Coupled Plasma Mass Spectrometry (ICP-MS) after a pre-concentration stage with nickel sulfide fire-assay collection. The CAS uses a modified NiS-fire assay method in which the samples are mixed with sodium carbonate, sodium borate, borax, glass powder, Ni powder, Fe powder, and S (Sun and Sun, 2005; Zhou et al., 2005). The precision of the analysis is better than 5% for Rh, Pd, and Ir, and 10% for the other elements. The detection limits are 0.2 ppb for Pt and Pd, 0.001 ppb for Ir, Rh and Os, and 0.1 ppb for Ru. A second batch of chromitite-dunite samples from the Sineh-Kar, Imam Hossein, Kermaniha Tunnel and Kalchenari-2 was analyzed at Genalysis Ltd (Perth, Western Australia) using nickel sulfide fire assay collection with ICP-MS finish following the method described by Chan and Finch (2001). In this analytical procedure, 25 g of sample is fused with a flux containing borax, soda ash, silica, nickel oxide, and sulfur. The sample material was fused at 1200 ºC to ensure all Cr-spinel grains were completely fused and that all PGE were collected by the nickel sulfide. The nickel sulfide button is dissolved with hydrochloric acid at ~100 ºC. The undissolved PGE sulfides and gold are collected on a cellulose nitrate membrane filter and digested with aqua regia in sealed borosilicate test tubes. The solution is diluted with 10% v/v nitric acid and thoroughly mixed. The final solution is analyzed using a Perkin-Elmer Sciex ELAN 6000 ICP-MS. Six calibrating standard solutions are used as standards and samples are spiked with two internal standards for drift monitoring. A certified reference material (South African Reference Material SARM-7) and in-house standards are included in every analysis batch. The measured PGE isotopes are ^{99}Ru, ^{101}Ru, ^{102}Ru, ^{103}Rh, ^{105}Pd, ^{106}Pd, ^{108}Pd, ^{189}Os, ^{193}Ir, ^{195}Pt, and ^{196}Pt. The results are corrected for interferences produced by Ni and Cu argides. Detection limits are 1 ppb for Rh and 2 ppb for all other PGE. Results are given in Table S5.

4. Results

4.1. Mineralogy and Texture

A classification criterium, developed by Greenbaum (1977) to describe the range of Cr-spinel and olivine modal proportions common in chromitiferous rocks, was used to distinguish between the Kuh-Siah chromite ore types (Table 1). Based on this classification, samples with modal proportion of Cr-spinel more than 90% chromite are massive, while 51-90% Cr-spinel is olivine-chromitite or semi-massive and 5-50% Cr-spinel is chromitiferous dunite or disseminated chromitites.

Microstructural observation reveals that individual Cr-spinel crystals in the Kuh-Siah chromitites vary in diameter from 0.1 mm to 10 mm. Generally, Cr-spinel grains are anhedral to euhedral. Grain edges in contact with interstitial silicates are straight, uneven or pitted. The silicate matrix within the ores is thoroughly altered to serpentine and chlorite. To various extents, ferrian Cr-spinel is observed in margins and within fractures of some Cr-spinels. Chromitite deposits situated in the locus of thrust faults are intensively deformed (Fig. 5a). Crack-seal networks due to intense brittle deformation are discernible in some chromitite samples (Fig. 5b). Microfractures are filled with calcite, serpentine, chlorite and andradite (Fig. 5b, 5c). In disseminated chromitites, anhedral Cr-spinels are irregularly clustered (Fig. 5d).

Cr-spinel in dunite enclosing all chromitites investigated here is predominantly anhedral to subhedral (Fig. 6a-c). In harzburgite associated with high Cr# spinel chromitite, the anhedral Cr-spinel crystals are associated with serpentinized orthopyroxene (Fig. 6d). In harzburgite-hosted low Cr# spinel chromitite vermicular spinel is in close association with small discrete clinopyroxene grains (Fig. 6e-f). Occasionally, large spinel grains occur as “holly-leaf”. In the Kalchenari-2 high-Al chromitite deposit, plates or coarse prismatic orthopyroxene contains exsolved clinopyroxene /magnetite needle-like crystals formed during cooling of both harzburgites and dunites, showing exsolution textures (Fig. 6c).

4.2. Silicate inclusions:

Euhedral quadrangular and round-shaped silicate inclusions consisting of clinopyroxene (Fig. 7b), orthopyroxene (Fig. 7c-d), Na-bearing phlogopite (Fig. 7e), serpentine or chlorite (Fig. 7f) are sporadically scattered within the Cr-spinel grains. These inclusions are mainly monophase minerals and rarely occur as polyphases. Silicate inclusions in Cr-spinel grains, mainly euhedral–subhedral in shape, are up to 20 μm in size.

4.3. Base Metal Minerals and Platinum Group Minerals

Grains, blebs (< 1 μm) and aggregates of base metal minerals (BMM) were found within massive chromitites and serpentinites of the Kuh-Siah massif. The BMM enclosed within Cr-spinel crystals are mainly euhedral Ni- and Cu-rich sulfides (5-10 μm), while others within the gangue are represented by small blebs of Ni-Fe alloys (up to 10 microns).

Platinum group minerals (PGM) are not widespread and were detected only inside Cr-spinel crystals within massive chromitites. The most widespread PGM are crystals of the laurite-erlichmanite series, but malanite and braggite were also detected.

The main Sineh-Kar chromitite hosts awaruites interstitial between Cr-spinel grains (Fig. 8a), while no sulfide was found within Cr-spinels.

The Kermaniha Tunnel chromitites are also PGM free and BMM poor, and copper sulfides (chalcocite) are only rarely found within the associated dunites (Fig. 8b). Within the Imam Hossein mine, chromitite BMM were found within Cr-spinel crystals (Fig. 8c), as single phases or as aggregates of Ni (polydymite, millerite) and Cu (geerite) sulfides (Fig. 8d).

Within the Ebrahim, Kalchenari-1, Kalchenari-3, Kalchenari-5 and Haj-Ghasem chromitite deposits, several PGM and BMM were detected. All the PGM and sulfides are enclosed within Cr-spinel, while in the silicate gangue only Ni-Fe alloys are recorded. The Kalchenari-1 mine chromitites are poor in sulfides, and only rare euhedral pentlandite grains of less than 10 microns are detected (Fig. 8e). Within nodular chromitite from the Kalchenari-3 deposit, millerite and chalcopyrite grains exist in unaltered Cr-spinel (Fig. 8f), while a polyphasic grain of Fe-Ni alloy and an unknown Co-Ni-Fe sulfide [probably Ni-Fe cobalt-pentlandite or bravoite] (Fig. 8g), occur in the silicate matrix interstitial between Cr-spinel. In disseminated chromitite from the Kalchenari-5 deposit, a heazlewoodite crystal occurs within unaltered Cr-spinel (Fig. 8h), while Fe-Ni alloys occur in the gangue. The Haj-Ghasem massive chromitites are rich in BMM and PGM. A polyphasic grain of millerite and bornite associated with clinopyroxene (Fig. 8i) and a polyphasic grain of laurite, millerite, Ni-rich braggite, BM-PGE sulfide and malanite (Fig. 7j) are recorded in unaltered Cr-spinel. In the silicate matrix, only Fe-Ni alloys are found. In the Ebrahim mine chromitites several laurite-erlichmanite crystals (Fig. 8k) occur in association with silicates (e.g., amphibole, talc) within unaltered Cr-spinel, along with rare millerite grains (Fig. 8l). Ni-Fe alloys once again occur only in the silicate matrix. In the Roholla New mine chromitites, only one laurite-erlichmanite grain (Fig. 8m) occurs along with an altered pentlandite grain that exists in a

partially ferrian-chromitized rim (Fig. 8n). Within the Kalchenari-2 deposit, an Ir-Rh-As sulfide grain is surrounded by an Fe-Ni alloy (Fig. 8o).

5. Mineral Chemistry

5.1. Cr-spinel:

The Kuh-Siah chromitite deposits are marked by spinels with contrasting and variable compositions. At outcrop scale, spinels from the Imam Hossein and Kalchenari-2 chromitites are high-Cr and high-Al end members of spinel composition, respectively. In the Kalchenari-2 deposit, chromitite sample is Al-rich with Cr# [(Cr/Cr + Al) × 100] lower than 60 and Mg# [(Mg/Mg + Fe^{2+}) × 100] ranging between 70-72 and Fe^{3+}# [(Fe^{3+}/Fe^{3+}+Cr + Al)] ranging between 2 and 4 (Table S1). The composition of pristine cores of the Cr-spinel in the Kalchenari-2 chromitites shows a lower variability in Cr_2O_3 (41.03–43.79 wt. %), Al_2O_3 (25.32–27.72 wt. %), MgO (15.52–16.08 wt. %), and total FeO (13.70–14.42 wt. %; Table S1). The contents of element oxides of Cr-spinel are low (TiO_2 ≤ 0.15 wt. %; MnO ≤ 0.09 wt. % and NiO = 0.19–0.28 wt. %; Table S1) and are generally analogous to those measured in the Cr-rich chromitites. In contrast, the Imam-Hossein chromitite sample is of Cr-rich type with high spinel Cr# (69–77) and Mg# (67–73). The Fe^{3+}# of these spinels varies between 1 and 4. The composition of Cr-spinels in the Imam Hossein chromitites shows significant variations in Cr_2O_3 (55.78–60.55 wt. %), Al_2O_3 (12.20–17.14 wt. %), MgO (14.43–15.93 wt. %) and total FeO (12.93–14.22 wt. %; Table S1). The minor element oxide concentrations in Cr-spinel of these chromitites are generally low (TiO_2 = 0.10–0.30 wt. %; MnO ≤ 0.14 wt. % and NiO ≤ 0.22 wt. %; Table S1). In general, all the Cr-spinel samples from the other chromitite deposits show intermediate compositions with unusually wide chemical differences at both outcrop and thin section scales but plot in the podiform field (Fig. 9). The Cr# of these intermediate spinels varies from 61 to 74 and Mg# from 57 to 72. The Fe^{3+}# [(Fe^{3+}/Fe^{3+}+Cr + Al)] of these spinels varies between 1 and 6. Minor amounts of MnO (>0.32 wt.%), TiO_2 (0.05–0.27 wt. %) and NiO (0.02–0.24 wt.%) are also detected. Cr-spinels in the dunite envelope of the investigated chromitites have composition similar to their chromitite bodies (Table S1).

In contrast to other chromitite deposits in the Kuh-Siah massif, the Cr# and Mg# values in Cr-spinel from the Kalchenari-2 chromitites are comparable with spinels from MORB lavas (Dick and Bullen, 1984; Fig. 9). Cr-spinel from dunite samples shows largely variable Mg# (40–78), compared to those from chromitites (Fig. 9c). In the TiO_2 vs. Al_2O_3 discrimination

diagram (Fig. 10a; Kamenetsky et al., 2001), the Kuh-Siah Cr-spinels plot in a progressive order with high-Al Cr-spinel in the MORB-type peridotite field progressing into the transitional MORB-type–SSZ-type peridotite and subsequently SSZ-type peridotite region as the Al_2O_3 content of the Cr-spinels decreases.

Cr-spinels from the Kuh-Siah chromitite and associated peridotites form a trend (Fig. 10b) from low Cr# and low TiO_2 wt. % compositions (close to the melting curve), to a trend with high Cr# and constant TiO_2 wt. % compositions, significantly displaced from the melting curve. Different stages of magmatic evolution of Cr-spinel can be observed based on the harzburgite composition from different Cr-spinel compositions (Imam Hosseim, Kalchenrari-3 and Kalchenari-2) (Fig. 10b).

5.2. Silicate inclusions:

Pyroxenes

The composition of orthopyroxene inclusions in Cr-spinel is mostly enstatitic (Fig.11a), with average Mg# [$Mg/(Mg+Fe_{tot})$] of 0.94. Orthopyroxene has Cr_2O_3, Al_2O_3 and TiO_2 contents of 0.93–0.98 wt.%, 0.86–1.12 wt.% and <0.04 wt.%, respectively (Supplementary Table S2). Clinopyroxene inclusions in Cr-spinel from the chromitites and associated dunite are diopside (Fig. 11a) and compositionally akin to those in accessory Cr-spinel in the dunite samples. They are marked by Mg# ranging between 0.92 and 0.96, high CaO contents ranging between 22.73– 24.60 wt.% (with average of 23.53 wt.%), low Al_2O_3 contents of 0.79-2.46 wt.% (with average of 1.51 wt.%) and Cr_2O_3 contents of 0.89 to 1.93 wt.% with average of 1.3 wt.% (Table S2). Cr-spinel-hosted clinopyroxene inclusions are characterized by Mg# ranging between 0.90 to 0.98, high CaO contents ranging between 22.80– 25.02 wt.% (with average of 24.45 wt.%), low Al_2O_3 contents of 1.3-2.61 wt.% (with average of 1.67 wt.%) and Cr_2O_3 contents of 1.20 to 2.31 wt.% with average of 1.66 wt.%.

Amphiboles

Based on the nomenclature of Leake et al. (1997), amphiboles show a wide range of compositions from tremolite-edenite to magnesio-hornblende and pargasite (Fig. 11b). They are characterized by Mg# between 0.91 and 1.00, TiO_2 contents between 0.25 and 0.78 wt. %, Cr_2O_3 contents between 2.66 and 4.07 wt. %, Na_2O varying between 2.90 and 4.43, and Al_2O_3 contents between 7.54-12.79 wt. % (Table S2).

Olivine

Journal Pre-proof

Olivine in the studied chromitites has unusually high forsterite contents varying between 95 and 97 mol.% which is akin to low-pressure olivines ($Fo_{91.5-96.5}$) in the Happo-O'ne (central Japan) prograde peridotites (Khedr and Arai, 2012) and low-pressure olivines ($Fo_{94.9-95.9}$) in the Korab Kansi (Egypt) prograde dunites (Khedr et al., 2022). They also resemble to extremely magnesian olivine from oxidized lavas of the Tolbachik Volcano (Kamchatka), chromitites from the Ray-Iz deposit (Russia), alkaline ultrabasic lavas from the San Venanzo volcanoes (Italy), and skarns from the Kuh-i-Lal deposit (Tajikistan) (Plechov et al., 2018). For olivines from the Kuh-Siah chromitites, the Cr_2O_3 contents vary from 0.20 to 0.80 wt.% (Table S2). Olivine relicts have high NiO contents (0.52-0.88 wt.%) and low MnO contents (0.04-0.09 wt.%).

Serpentine

Serpentine inclusions in Cr-spinel from chromitites are characterized by variable FeO (0.82-6.24 wt.%), MgO (33.93-41.43 wt.%), Cr_2O_3 (0.04-2.79 wt.%) and Al_2O_3 (0.06-1.84 wt.%) contents. The Mg# of these serpentine inclusions ranges between 0.91 and 0.99 (Table S2)

Chlorite

Generally, chlorite inclusions in Cr-spinel from the investigated chromitites display low FeO (<2.69 wt.%), high MgO (34.13-36.92 wt.%) and variable Cr_2O_3 contents (0.16-3.30 wt.%). They are marked by high Mg# varying from 0.96 to 0.99 (Table S2).

6. Bulk-rock PGE content

Bulk-rock PGE contents (85–537 ppb; Table S4) is in the range ascribed to ophiolitic chromitites (<1000 ppb total PGE; Leblanc, 1991; Gervilla et al., 2005; Ismail et al., 2010). The Ir /(Pt+Pd) ratio is rather low in high-Al chromitites compared to high-Cr chromitites. The chondrite-normalized PGE contents of the high-Cr and -Al samples exhibit an enrichment in IPGE (Os, Ir and Ru) relative to PPGE (Rh, Pt and Pd).

The Kuh-Siah dunites are enriched in PGE relative to the upper mantle (McDonough and Sun, 1995), but depleted relative to the associated chromitites (Table S4). Dunite samples from Imam Hossein and Kermaniha Tunnel deposits show positive Ir and negative Ru anomalies.

According to classification of Burgath et al. (2002), most of the Kuh-Siah chromitites and dunites have group-I PGE patterns characterized by $Pt_n/Ir_n<0.9$ and $Pt_n/Pd_n<1$, representing the "normal ophiolite type" (Fig. 12a). Other samples have $Pt_n/Pd_n>1$ (up to 20) and PGE total up to 1.5 ppm and are classified here as group-I* (Fig. 12b).

Journal Pre-proof

There is no correlation between PGE abundance and Cr# in the Kuh-Siah chromitites (Fig. 12c).

PGE contents of the studied chromitites and associated dunites were not controlled by differentiation of the parental magma (Fig. 12d). The Kuh-Siah chromitites were not simply derived from partial melting of the mantle peridotite.

Generally, patterns for both high-Al and high-Cr chromitites display a negative Pt anomaly ($Pt_n/(Rh_n \times Pd_n)^{½}$ =0.03–0.73). It is crucial to note that high-Al chromitite sample exhibits higher Pt anomaly (0.73) resulting in gentle slope in PGE-normalized pattern (Fig. 13).

7. Discussion:

7.1. Heterogeneity in Cr-spinel composition and controls on PGE signatures

The investigated chromitite deposits with contrasting and variable composition coexist within a single peridotite massif, and this chemical heterogeneity can also be tracked over small distances. For example, the distance between Kalchenari-2 high-Al chromitite deposit and Kalchenari-3 is less than 200 meters (Fig. 2b). High-Al chromitite orebodies strike NW akin to high-Cr chromitite orebodies. As discussed above, this heterogeneity, at a scale of a few hundred meters, is not related to the changing tectonic settings. Based on the chemistry of primary Cr-spinel in the Kuh-Siah chromitites, the chemistry of parental melts is a main factor in controlling heterogeneity at shorter scales.

High-Al chromitites in ophiolitic complexes occur in the mantle section or in the cumulate rocks above Moho. High-Al chromitites within the mantle section are usually poor in PGE and are formed at subduction initiation from magmas with MORB affinity (Chen et al 2019). High-Al chromitites in the cumulate rocks above Moho can be associated to pyroxenite and wehrlite layers (Garuti et al., 2012). They usually consist of massive aggregates with cumulative textures, and often include high PGE contents (> 3000 ppb total PGE content) (Zaccarini et al., 2004; Grieco et al., 2007; Bussolesi et al., 2022). In the Kuh-Siah, high-Al and high-Cr chromitites are observed only in the mantle section and they do not show any clear textural differences. In this massif, both high-Cr and high-Al chromitites have relatively moderate PGE contents (mean~250 ppb). This implies that melting of the mantle peridotite was sufficient to enter the critical melting interval for the effective removal of PGE. Arc-related melts, which originate above the subduction slab in ophiolite settings, are

created by moderate to high partial melting degrees (i.e., 20% melting) that result in nearly full dissolution of mantle sulphides and basaltic melts enriched in PGE. As a result, the chromitites that are formed in equilibrium with these melts frequently contain PGE in concentrations ranging from a few hundred to thousands of parts per billion (e.g. Zhou et al., 1998; Proenza et al., 1999; González-Jiménez et al., 2011). Regardless of their PGE contents, both high-Cr and high-Al chromitites show a systematic enrichment in IPGE relative to PPGE. This is confirmed by the predominant occurrence of minerals of the laurite–erlichmanite solid solution series in the Kuh-Siah chromitites. During percolation of melts through depleted mantle and subsequent melt-rock reactions, residual sulfides (enriched in Os, Ir and Ru, but moderately depleted in Rh, Pt and Pd) were extracted from the mantle and their fractionated PGE nature must have been transferred to the migrating parental melts responsible for chromitite formation (e.g. Bockrath et al., 2004; González-Jiménez et al., 2011). This process can explain the similar PGE patterns of the two chromitite varieties. Covariation of Pd/Ir with Pt/Pt* [$Pt_n/(Rh_n \times Pd_n)^{1/2}$] for the studied samples (Fig. 12d) reveals that the PGE content in the Kuh-Siah chromitites was controlled by partial melting rather than magma fractionation. This also suggests a polygenetic origin for the formation of these chromitites (e.g., Tzamos et al., 2017; Uysal et al., 2018). The absence of correlation between PGE content and Cr# (Fig. 12c) precludes the possibility of metasomatic melt-rock reaction as a factor controlling the PGE concentrated in the Kuh-Siah chromitites. This is also verified by a scarcity of base metal sulfides as well as the highly depleted nature of the Kuh-Siah mantle peridotites. Additionally, it is consistent with the very restricted range of TiO_2 contents of parental melts of chromitites (e.g. Uysal et al., 2018).

7.2. Textures formed by subsolidus exsolution or melt-rock reaction

Textures produced during cooling observed in this study include spinel-pyroxene symplectite aggregates as well as exsolution of spinel-clinopyroxene lamellae from olivine and orthopyroxene (Fig. 6c-6f). Four hypotheses have been put forward to explain the spinel-pyroxene symplectite aggregates: (i) breakdown of garnet (e.g. Vannucci et al., 1993; Morishita and Arai, 2003; Rampone et al., 2009); (ii) melt-rock reactions and crystallization of mineral phases from a melt (e.g. Seyler et al., 2007; Suhr et al., 2008; Godard et al., 2008) and (iii) subsolidus exsolution of spinel from the pyroxene host during cooling and intercrystalline Mg-Fe exchange (e.g. Kuo and Essene, 1986; Field and Haggerty, 1994; Rampone et al., 2008). (iv) a reaction between a pre-existing garnet and percolating fluids during cooling (e.g. Godard and Martin, 2000; Forster et al., 2017). The Cr-spinel in the

symplectite aggregates occurs as vermicular grains closely intertwined with clinopyroxene in the investigated harzburgite-hosted high-Al chromitites (Fig. 6f). These Cr-spinels may have formed through the reaction between Cr-rich orthopyroxene and olivine during melting and mantle upwelling processes. In these harzburgites and associated dunites, needle-shaped lamellae of spinel (Fig. 6c) may have exsolved in olivine and orthopyroxene porphyroclasts during cooling and decompression (Arai 1978; Franz and Wirth, 2000; Li et al., 2015). On the contrary, the idiomorphic morphology of Cr-spinel in the harzburgite hosted high-Cr chromitite can be ascribed to the interaction between residual mantle peridotites and percolating Si- undersaturated melts (e.g. Kelemen et al., 1995; Park et al., 2022).

7.3. Mantle oxidation state during evolution of chromitites

Several studies have shown that specific oxidation processes may lead to a non-stoichiometric composition of Cr-spinel crystals. Deviation from stoichiometry can be characterised by a combination of analytical techniques, including X-ray single crystal diffraction, Mössbauer spectroscopy and electron microprobe analyses. Comparison of the $Fe^{3+}/\Sigma Fe$ ratios as derived from these methods sometimes show deviating ratios, which is an effect of non-stoichiometry. Noteworthy, a balanced stoichiometric formula can still be calculated from solely electron microprobe analyses, but would lead to an erroneous $Fe^{3+}/\Sigma Fe$ ratio.

Cr-spinel is a normal spinel, i.e. with divalent cations mostly in the tetrahedral site and trivalent cations in the octahedral site. During oxidation, following a reaction that could be simplified as $3Fe^{2+} \rightarrow 2Fe^{3+} + \square$, where $\square$ represents a vacancy, ferrous iron in T site can be replaced by ferric iron, followed by oxidation of, possibly scarce, ferrous iron in the M site (Carbonin et al. 1999; Bosi et al. 2004; Derbyshire et al. 2013; Lenaz et al. 2004, 2014a, 2014b; Rollinson et al., 2017). This mechanism is consistent with the observations by Mattioli and Wood (1988) and Ghiorso and Sack (1991) that showed in their thermodynamic models how vacancies can be randomly distributed across the T and M sites in the spinel structure. A visible effect is the formation of a so-called ferrian Cr-spinel rim, even if the way it develops and the enrichment or depletion of different cations and their exchange with the environment are still a matter of debate due to exchange with other mineral phases present in the surrounding environment (see Mellini et al., 2005; Gonzalez-Jimenez et al., 2005, 2009; Merlini et al., 2009, among others, for details). Similar changes have been observed in laboratory experiments on both natural and synthetic spinels (Velicogna and Lenaz, 2017; Lughi et al., 2020).

Journal Pre-proof

Because of the oxidation process, there will be a large discrepancy in the $Fe^{3+}/\Sigma Fe$ ratios based on results from EMPA and Mössbauer spectroscopy, typically with a higher ratio for the Mössbauer results. In the past years, several papers dealt with this problem and suggested that this oxidation phenomena are related to post-magmatic processes (Carbonin et al., 1996; Li et al., 2002; Quintiliani, 2005; Quintiliani et al., 2006; Rollinson et al., 2012, 2017; Adetunjii et al., 2013; Lenaz et al., 2013, 2014a, 2014b, 2018).

Figure 14 shows a comparison between the $Fe^{3+}/\Sigma Fe$ ratio calculated via MS and EMPA. There are three samples, SI2, KE2 and IM, where the difference is twice to 3.5 higher in the conventional MS results with respect to EMPA. In the same figure are also plotted samples from other occurrences where a non-stoichiometry has been identified [ophiolites from Albania (Bosi et al., 2004; Quintiliani et al., 2006), India (Lenaz et al., 2014b), Oman (Rollinson et al., 2012; Lenaz et al., 2014a), Amsaga Archean complex in Mauretania (Lenaz et al., 2018) and the Bushveld layered complex (Adetunjii et al., 2013; Langa et al., 2021)]. As stated by Lenaz et al. (2013), there could be large discrepancies in the $Fe^{3+}/\Sigma Fe$ ratio measured via conventional MS analyses compared to point-source MS. This may occur as a larger amount of material is needed for conventional MS in which the $Fe^{3+}/\Sigma Fe$ ratio may be very different (especially if ferrian Cr-spinel rims are diffuse), while point-MS can be performed with a very small amount of material (normally < 1mg). We adopted both methods for two of the samples (SI-2C and KE-2) that showed anomalously high $Fe^{3+}/\Sigma Fe$ ratios to compare the results. As shown in Figure 14, there is a large difference for one of the samples ($Fe^{3+}/\Sigma Fe$ ratio equal to about 32% for conventional MS vs. about 29% for point-source-MS) while for the other the difference is limited. These results, consequently, confirms that the point-source technique can provide better results for altered or otherwise heterogeneous samples.

Considering the similarity between the here studied chromitites and those from Oman (Rollinson, 2008; Rollinson et al., 2012; Lenaz et al., 2014a), it can be suggested that the localized oxidation may be linked to dominant hydrous fluids existing in the shear zone or shear deformation as all the three occurrences are close to each other and located in the SW shear system area (Fig. 2). As regards the non-oxidized samples, their $Fe^{3+}/\Sigma Fe$ ratios are fairly similar within the range 0.15-0.20. These values resemble those of other ophiolites like those of the Indo-Myanmar (India; Lenaz et al., 2014b) and Leka (Norway; O'Driscoll et al., 2021) occurrences.

Journal Pre-proof

7.4. Composite origins inferred from Cr-spinel-hosted solid inclusions

7.4.1. Silicate inclusions

There have been four main lines of thought related to the origin of chromite-hosted silicate inclusions: (i) post-magmatic entrapment of already-formed silicate phases during sub-solidus sintering of chromite, accompanied by interaction with hydrothermal fluids (e.g., Hulbert and Von Gruenewaldt, 1985), (ii) entrapment of anhydrous liquidus silicates in the presence of fluids or volatile-rich liquids contemporaneously with chromite growth (e.g., Lorand and Ceuleneer, 1989; McElduff and Stumpfl, 1991), (iii) closed-system cooling of volatile-rich melts inside chromite as a consequence of melt-peridotite interaction and melt mixing (e.g., Arai et al., 1997; Melcher et al., 1997; Schiano et al., 1997; Morishita et al., 2011; Khedr and Arai, 2016), (iv) precipitation from super-critical fluids (e.g., Dmitrenko and Mochalov, 1989; Johan et al., 2017).

In general, chromite-hosted silicate inclusions in the Kuh-Siah samples contain olivine, orthopyroxene, Cr-diopside, pargasite-hornblende, tremolite-edenite, chlorite and serpentine (Fig. 7). Inclusions located near fractures/cracks or in highly deformed chromite grains often comprise tremolite, chlorite, serpentine and secondary garnet (Fig. 7e-f). Their large size due to connection with outside spinel grains and anhedral to subhedral fiber or flaky shapes with heterogeneous compositions, suggest a secondary origin. However, inclusions found in visually pristine areas or fresh cores of chromite crystals often comprise unaltered orthopyroxene, clinopyroxene and amphibole (Fig. 7a-d); therefore, they may be considered as unaltered, pristine inclusions. These inclusions are mainly globular in shape, monophasic and unconnected to cracks and/or spinel grain boundaries. They are considered as primary mineral inclusions, formed during spinel formation. If a group of such inclusions exists in a single grain, their boundaries are parallel to each other (Fig. 7f), indicating negative crystal shapes, i.e., they are aligned according to the crystallographic orientation of the host. This may be explained in different ways:

a) The host crystal crystallized before the minerals of inclusions, hence, the latter crystallized in-situ (i.e., as portions of crystallizing melt).

b) Inclusions formed as a result of the grain boundary migration due to the subsolidus sintering or annealing (e.g., Satsukawa et al., 2015).

The first possibility may be used to explain the origin of multimineralic assemblages that are often interpreted as melt inclusions (Spandler et al., 2005; Rollinson et al., 2018; Yao et al., 2022); however, monomineralic inclusions cannot be explained in this way. The alternative

explanation is that these minerals crystallized simultaneously with Cr-spinel. This is supported texturally: detailed observation of the shape of the inclusion reveals that while being subordinate to the general pattern dictated by the host mineral, each inclusion comprises its own euhedral face (Fig. 7a-d). Therefore, one of the possible explanations is that Cr-spinel precipitated together with amphibole, which implies a hydrous nature of the melt responsible for this process.

The second possibility also explains the observed textural peculiarities and may be considered as an additional post-magmatic stage that contributed to the formation of chromitites as they currently are.

Another interesting property of the inclusions is the high Cr contents (up to 3 wt % Cr_2O_3) in some of the pyroxenes and amphiboles (Table S2), that cannot be attributed only to secondary fluorescence contribution. Hence, these phases indicate that both Cr-spinels and silicates crystallized from a medium enriched in Cr. Together with the data on the hydrous nature of the inclusions, this may be taken as evidence of chromitite formation from hydrous, extremely Cr-rich melts followed by possible recrystallization and hydrothermal alteration. The presence of orthopyroxene and olivine inclusions does not contradict a boninitic nature of the supposed melt.

7.4.2. Ni-Fe-Cu base metal minerals

Primary BMM within the Kuh-Siah chromitites and associated rocks (Fig. 8) are constituted by sulfides found enclosed within unaltered Cr-spinel. Pentlandite, pyrrhotite, bornite and chalcopyrite are the most common primary sulfides detected within ophiolite hosting chromitites (e.g. Proenza et al., 2001; González-Jiménez et al., 2010; Derbyshir et al., 2013), and their textural shape in the Kuh-Siah chromitites confirms their primary origin. They are formed upon the separation of an immiscible sulfide melt during the early stages of crystallization of basic magmas, forming pyrrhotite, chalcopyrite and later pentlandite. Pentlandite is formed when pyrrhotite breaks down below 610 °C, forming either a pentlandite-pyrrhotite association or a pentlandite-heazlewoodite association (below 550 °C), depending on the metal to sulfur ratio (Kullerud, 1963). Pyrrhotite will dissolve in chalcopyrite above 300 °C (Hewitt, 1938). Heazlewoodite, millerite and Ni-Fe alloys are the most common secondary sulfides in ophiolite chromitites, being the result of a desulfurization processes (Klein and Bach, 2009). The alteration of pentlandite into heazlewoodite occurs below 550 °C, while the formation of Ni-Fe alloys has been estimated to occur below 445 °C, at low fO_2 and fS_2 (Tzamos et al., 2016). Heazlewoodite can be

replaced by millerite if fO_2 and fS_2 increase, like during steatitization of ultramafic rocks (Klein and Bach, 2009). Millerite, commonly classified as a secondary sulfide, has been also thought to crystallize at magmatic temperatures (González-Jiménez et al., 2020, 2012; Uysal et al., 2009). The textural position of millerite in the Kuh-Siah chromitites, completely enclosed in unaltered Cr-spinel, supports an origin at higher temperatures. Experiments by Kullerud and Yund (1962) highlight the existence of a high-T polymorph of the mineral millerite ($\alpha Ni_{1-x}S$) stable at high temperatures (~1000 °C), and transitioning into stoichiometric millerite at ~380 °C.

The alteration of pentlandite into heazlewoodite and awaruite detected in the Kuh-Siah chromitite samples (Fig. 15a) is a common feature in serpentinized ultramafic rocks (Frost, 1985), and can be attributed to a desulfurization event due to the circulation of low fS_2 – low fO_2 serpentinizing fluids (Garuti and Zaccarini, 1997; Gonzalez-Jimenez et al., 2011; Grieco et al., 2020; Prichard et al., 1994). During serpentinization of the ultramafic rocks, primary Co-pentlandite is altered to heazlewoodite during reducing conditions. The Ni content of awaruite is possibly derived from olivine and Co-pentlandite (Tzamos et al., 2016*)*. The reducing environment resulting from serpentinization and the low sulphur fugacity favors the formation of awaruite, heazlewoodite and magnetite (Tzamos et al., 2016*)* (Fig. 8). A desulfurization trend can also be seen in the Cu sulfide assemblage in which removal of sulfur resulted in reduced assemblages (Fig. 15b). Ni-Fe alloys are particularly enriched in the Sineh-Kar and Kalchenari deposits. This is in agreement with mantle oxidation data, which suggest a local oxidation at these localities, with consequent formation of ferrian Cr-spinel by oxidation of ferrous iron into ferric iron (e.g., serpentinization) (Klein and Bach, 2009). This produces extremely reducing conditions, which in turn favor the stabilization of native metals and alloys by desulfurization of primary and/or secondary sulfides.

7.4.3. Platinum Group Minerals

PGM in the Kuh-Siah chromitites were detected only in three mining areas including the Haj-Ghasem, Ebrahim and New Rohollah deposits. All the PGM are primary sulfides enclosed within unaltered Cr-spinel, and no PGE-alloy was detected. As is common for ophiolite chromitites, the most abundant PGM belong to the laurite-erlichmanite series (Fig. 16a) (González-Jiménez et al., 2014 and references therein). Stoichiometric laurite crystallizes from the silicate melt at 1200-1300 °C or even from sulfide undersaturated melts (Andrews and Brenan, 2002; Bockrath et al., 2004; Brenan and Andrews, 2001). With decreasing

temperature and/or increasing fS_2, Os and Ir become more soluble in the laurite lattice, producing minerals with compositions within the laurite-erlichmanite series (Brenan and Andrews, 2001). Os and Ir contents within laurites therefore suggest a crystallization in a dynamic regime, which can be achieved with an increase in fS_2 upon cooling, or by mixing of different melts (Gonzalez-Jimenez et al., 2014). Gonzalez-Jimenez and Reich (2017) also argued that mixing of melts within conduits in the upper mantle, changes in fS_2, fO_2 and Ru/(Os + Ir) ratios are factors controlling the fractionation between Os-Ir-Ru and Pt-Pd.

In one chromitite sample, a polyphasic grain composed of laurite, millerite, malanite, braggite and a BM-PGE sulfide has been detected (Fig. 8). Malanite is a thiospinel PGM with general formula $Cu^{1+}(Ir^{3+}Pt^{4+})S_4$, in which the predominant PGE is Pt. Braggite, ideally (Pd, Pt)S, is fairly common in both stratiform and podiform chromitite deposits. BM-PGE sulfides have been identified in podiform chromitites from Kraubath (Malitch et al., 2001) and in the Kempirsai chromitite deposits (Melcher et al., 1997). Melcher et al. (1997), in particular, have detected a close association of BM-PGE sulfides with millerite, and suggested the presence of a high temperature PGE-BM solid solution of the millerite type, that would become unstable with cooling, forming stoichiometric millerite and platinum group minerals. The polyphasic grain found in the Kuh Siah chromitite samples (Fig. 8j) implies a similar origin. From a S-BM-PGE-rich droplet trapped in a Cr-spinel crystal, the first phase likely to crystallize is laurite, subtracting Ru and Os from the melt. From the textural observation, the second phase crystallized is braggite (Pt, Pd, Ni)S, consuming all Pd and part of Pt. Braggite may crystalize at magmatic temperatures of 1000°C (Cabri et al., 1978), and its Ni content is a function of temperature. Further cooling resulted in the crystallization of millerite, and the unmixing between malanite and the BM-PGE sulfide, clearly visible from the BSE image (Fig. 8j).

Whole rock PGE normalized patterns are consistent with the mineral chemistry and show a positive Ru peak. As no PGE alloy was detected, we can assume that desulfurization only affected the base metal minerals, while PGM, enclosed within Cr-spinel, did not come in contact with the alteration fluids.

7.5. Genetic model for the formation of chromitites

There is general consensus that high-Al chromitites and high Cr-chromitites in ophiolites may crystallize from melts of MORB and boninitic affinities, respectively. Boninitic magmas contain ~ 200–1800 ppm Cr (e.g. Hickey and Frey, 1982) whereas MOR averages show much lower Cr content ranging from 81 to 406 ppm (Gale et al., 2013). These low Cr

contents are not adequate to form economic scale chromitite deposits in ophiolites. Thus, an extensive accumulation of Cr-spinels cannot be attributed to a direct crystallization of Cr-spinel from these MOR basaltic melts and a highly efficient mechanism would be required to accumulate Cr spinels. The most prominent model used by Irvine (1977) suggested that the mixing of two consanguineous melts with subsequent pulses of primitive mantle-derived melt might trigger the Cr-spinel oversaturation in the melt. Some models considered the mixing of primitive melts with alkaline and reduced fluids as a potential mechanism for the formation of chromitites (Talkington et al., 1984; Whittaker and Watkinson, 1984). Moreover, ophiolitic chromitites were thought to have originated as a result of interaction of a reduced fluid with vapor-rich magmas at ~ 1000 °C and 2–5 kbar under low oxygen fugacity (Johan, 1983, 1986). Arai and Abe (1995) adopted the model previously put forward by Irvine (1977) and suggested that a reaction between orthopyroxene with high Cr# and alkali-basaltic melt is accountable for the formation of podiform chromitites. We also accept this model for the investigated chromitites due to presence of hydrous euhedral silicate inclusions in the Cr-spinels. Furthermore, González-Jiménez et al. (2014) suggested that ophiolitic chromitites are formed by disequilibrium Cr-spinel precipitation, which is induced by small-scale mingling of melts with different SiO_2 contents derived from a heterogeneous deeper mantle source.

A critical aspect of all contemporary models for the genesis of ophiolitic chromitites is the role of metasomatic, pneumatolithic, or hydrothermal processes (Akizawa and Arai, 2014; Arai and Akizawa, 2014; Johan et al., 2017; Su et al., 2020; Arai, 2020). The indispensable role of water in chromitite formation has been highlighted in several studies (e.g. Johan et al., 1983; McElduff and Stumpfl, 1991; Matveev and Ballhaus, 2002; Johan et al., 2017; Rospabé et al., 2019; Su et al., 2020; Arai et al., 2020). Mobility of chromium in aqueous systems under low temperature conditions remains doubtful and is the subject of ongoing debate. Compared to aqueous alkali carbonate or silicate solutions, low pH chloride fluids are more capable to mobilize and transport Cr^{3+} at crustal conditions (Watenphul et al., 2014). High temperatures and reducing conditions favor high solubility of Cr^{2+} (cf. Borisova et al., 2012). The solubility of chromium in high temperature deep crustal and upper mantle fluids has been previously investigated (e.g. Akizawa et al., 2016; Johan et al., 2017; Huang et al., 2019). Huang et al. (2019) suggested that Cr solubility in high-T fluids is profoundly dependent on oxygen fugacity and Cl concentration. Their thermodynamic modelling predicts that reducing, Cl-bearing, subduction zone fluids show higher Cr solubility compared to the crustal mid ocean ridge hydrothermal fluids. In spite of the high mobility of chromium under

specific circumstances discussed above, it is not perspicuous whether a significant amount of newly formed Cr spinel may form during metamorphic processes or not.

The understanding of geodynamic settings for the formation of ophiolitic chromitites remain controversial. Due to the scarcity of large chromitite bodies in the contemporary ocean floor, a sub-arc magmatic setting has been suggested as a more favorable geodynamic environment for the formation of ophiolitic chromitites (g., Arai and Yurimoto, 1995). On the other hand, Arai and Miura (2015) argued that podiform chromitites may form within oceanic upper mantle beneath fast-spreading centers or the segment center of slow-spreading centers, where refractory harzburgite hosting spinels with Cr# 40–60, is a common component. It is commonly believed that there is a direct link between Cr-spinel composition of ophiolitic chromitite and its geodynamic setting. The high-Cr# /low-Ti Cr-spinel and low-Cr# /high-Ti Cr-spinel compositions of the Kuh-Siah peridotite massif (Figs. 9 and 10; Table S1) reflect their equilibrium with boninitic magmatism in the forearc and MORB in mid-ocean ridge and back-arc basin settings, respectively (e.g., Zhou et al., 1998, Zhou et al., 2014, Uysal et al., 2009, González-Jiménez et al., 2011, Robinson et al., 2015, Arai and Miura, 2016; Khedr and Arai, 2016, 2017).

Formation of Cr-spinel with intermediate composition has also been attributed to a tholeiitic melt with intermediate affinity during the early stage of subduction initiation in a proto-forearc setting (e.g. Moghadam et al. 2015; Khedr and Arai, 2016, 2017; Uysal et al. 2018; Kapsiotis et al. 2019; Liu et al. 2019; Chen et al. 2019; Sepidbar et al. 2021). Therefore, the substantial compositional variation in Cr-spinel from the IBM forearc mantle is assumed to be due to a transition in melt composition from MORB-like to boninitic (e.g. Morishita et al., 2011, Zhang et al., 2016), like the investigated chromitites.

Very short distances (~200 meters) between the investigated high-Al and high-Cr chromitite occurrences in a single peridotite massif, rule out any possibility for abrupt switch of tectonic settings. Instead, progressive evolution of melt composition in a single geodynamic setting is more likely. It is significant to mention that the low TiO_2 content of pristine Cr-spinel in the refractory chromitites with high Al_2O_3 from the Kalchenari-2 deposit (Table S1) does not support a true MOR or a back-arc basin (BAB) origin for their parental magmas (e.g, Rollinson, 2008; Zhou et al., 2014). These chromitites show transitional composition between MORB and boninitic melts. A plausible explanation for the occurrence of these high-Al and low Ti chromitites is their formation via tholeiitic melt through proto-forearc spreading and evolution of an infant arc. This interpretation can be corroborated by the geodynamic evolution of the Sabzevar ophiolite, which suggests a progressive shift from infant to mature

arc stages during late Cretaceous (Shafaii Moghadam et al. 2014). High-Cr chromitites in the Kuh-Siah peridotite massif, characterized by high Cr#, 77–80, and Mg#, 67–71, and low Al_2O_3 and TiO_2 contents (Figs. 10a, 10b), are in equilibrium with the compositions of Cr-spinel crystallized from boninitic melts in mature forearc ophiolites. The crustal sequence of the Sabzevar ophiolite is marked by supra-subduction zone (SSZ)-type volcanic and plutonic rocks (Shafaii Moghadam et al., 2014), which could be considered as differentiated counterparts of the parental melts of the chromitite deposits in this ophiolite.

7.6. Nature of processes promoting compositionally heterogeneous Sabzevar chromitite formation

The substantial compositional differences of Cr-spinel in the Kuh-Siah chromitites are assumed to be due to a transition in magma composition from MORB-like to boninite-like similarly to the Izu–Bonin–Mariana (IBM) forearc mantle, (e.g. Morishita et al., 2011; Zhang et al., 2016; Khedr et al., 2016, 2017). Our petrographic observations and geochemical interpretations reveal that the chromitites in the Kuh-Siah peridotite massif were formed during a multistage melt/fluid-peridotite reaction process in an extended intra-oceanic arc–forearc setting between the Turan and Central Iran continental blocks in the Mid to Late Cretaceous (Fig. 17). During the early stage, MORB-like to island-arc tholeiitic magmatism developed as a result of continuing subduction and fast rollback of the subducting slab, resulting in primitive formation of protoarc crust. The subducting oceanic slab was a MORB-type lithosphere generated earlier than Albian. High-Al, low-Ti Cr-spinels were generated from tholeiitic melts in a proto-forearc mantle during the infant arc stage. A prompt slab rollback induced extension and consequently fore-arc splitting, resulting in increasing asthenospheric diapiric upwelling and arc-wedge corner flow. During this stage, high degrees of partial melting generated an ultra-depleted residual harzburgite and boninitic-like melt segregation. The hydrous nature of the euhedral silicate inclusions (mainly amphibole) enclosed in Cr-spinel grains in the Kuh-Siah chromitite ruled out the possibility of their precipitation from an anhydrous primitive basaltic or boninite-like melts. Therefore, at the final stage of the arc magmatism system, high-Cr spinel precipitated from a melt hybrid between common mafic melts and more exotic Si-, Na- and volatile-rich fluids. A significant contribution of slab-derived fluids is responsible for the formation of the Kuh-Siah high-Cr chromitites (Shafaii Moghadam et al., 2015). Both high-Al and high-Cr chromitites are thought to be formed through the reaction between mantle-derived olivine-Cr-spinel saturated or hybrid melts and surrounding mantle peridotites which result in formation of small melt

conduits or interconnected 3-dimensional networks of film-like channels in the mantle sections of ophiolites (e.g. Arai and Yurimoto, 1994; Zhou et al., 1994; González-Jiménez et al., 2014).

Subsequently, subsolidus re-equilibration resulted in partial modification of the Cr spinel composition (low Mg# at high Cr#) and formation of cooling textures. During the post-solidus stage, already-formed silicate phases (Fig. 7) entrapped at the time of grain boundary migration due to subsolidus sintering or annealing. At this stage, low fS_2 – low fO_2 serpentinizing fluids circulated through the system resulting in desulfurization of sulfide mineral phases and alteration of Cr-spinel (Eslami et al., 2021; Eslami et al., 2023).

8. Concluding remarks

Based on textural observation, chemical analyses and oxygen fugacity measurements, the Kuh-Siah chromitite deposits have formed during a multistage melt/fluid-peridotite reaction process in an extended intra-oceanic arc–forearc setting between the Turan and Central Iran continental blocks in the Mid to Late Cretaceous. Ti-poor high-Al chromitites in the Sabzevar ophiolite originated from a nascent forearc mantle during subduction initiation. High-Cr chromitites formed through the reaction between mantle-derived hybrid melts and surrounding mantle depleted peridotites, which resulted in the formation of small melt conduits or interconnected 3-dimensional networks of film-like channels in the uppermost part of the mantle section. Field observations and textural studies revealed the localized post-magmatic oxidation may be linked to dominant hydrous fluids existing in the shear zone or shear deformation.

Acknowledgments

The authors are grateful to Kavandegan Bana Chromite Mining Development Company for logistical assistance during the fieldwork. The authors also thank Ali Polat for his editorial handling of our manuscript. Two anonymous reviewers are thanked for thoughtful and insightful reviews which substantially improved this contribution.

Conflicts of interest

Journal Pre-proof

We declare no conflict of interest. The funding sponsors had no role in the design of the study, in the collection, analyses or interpretation of data, in the writing of the manuscript, and in the decision to publish the results.

Journal Pre-proof

References

Adetunji, J., Everitt, S., Rollinson, H., 2013. New Mössbauer measurements of $Fe^{3+}/\Sigma Fe$ ratios in chromites from the early Proterozoic Bushveld Complex, South Africa. Precambrian Research 228, 194–205.

Ahmed, A. H., Arai, S., 2002. Unexpectedly high-PGE chromitite from the deeper mantle section of the northern Oman ophiolite and its tectonic implications. Contributions to Mineralogy and Petrology 43(3), 263–278.

Akizawa, N., Tamura, A., Fukushi, K., Yamamoto, J., Mizukami, T., Python, M., Arai, S., 2016. High-temperature hydrothermal activities around suboceanic Moho: An example from diopsidite and anorthosite in Wadi Fizh, Oman ophiolite. Lithos 263, 66–87.

Akmaz, R. M., Uysal, I., Saka, S., 2014. Compositional variations of chromite and solid inclusions in ophiolitic chromitites from the southeastern Turkey: Implications for chromitite genesis. Ore Geology Reviews 58, 208–224.

Aldanmaz, E., Meisel, T., Celik, O. F., Henjes-Kunst, F., 2012. Osmium isotope systematics and highly siderophile element fractionation in spinel-peridotites from the Tethyan ophiolites in SW Turkey: Implications for multi-stage evolution of oceanic upper mantle. Chemical Geology 294–295, 152–164.

Andrews, D. R. A., Brenan, J. M., 2002. Phase-equilibrium constraints on the magmatic origin of laurite + Ru-Os-Ir alloy. Canadian Mineralogist 40(6), 1705–1716.

Arai, S., Abe, N., 1994. Podiform chromitite in the arc mantle: chromitite xenoliths from the Takashima alkali basalt, Southwest Japan arc. Mineralium Deposita 29(5), 434–438.

Arai, S., Abe, N., 1995. Reaction of orthopyroxene in peridotite xenoliths with alkali-basalt melt and its implication for genesis of alpine-type chromitite. American Mineralogist, 80(9–10), 1041–1047.

Arai, S., Yurimoto, H., 1994. Podiform chromitites of the Tari-Misaka ultramafic complex, southwestern Japan, as mantle-melt interaction products. Economic Geology 89(6), 1279–1288.

Arai, S., Yurimoto, H., 1995. Possible subarc origin of podiform chromitites. The Island Arc 4, 104–111

Arai, S., 1978. Chromian spinel lamellae in olivine from the Iwanai-dake peridotite mass, Hokkaido, Japan. Earth and Planetary Science Letters 39(2), 267–273.

Journal Pre-proof

Arai, S., Akizawa, N., 2014. Precipitation and dissolution of chromite by hydrothermal solutions in the Oman ophiolite: New behavior of Cr and chromite. American Mineralogist 99(1), 28–34.

Arai, S., Miura, M., 2016. Formation and modification of chromitites in the mantle. Lithos 264, 277-295.

Arai, S., Miura, M., 2015. Podiform chromitites do form beneath mid-ocean ridges. Lithos 232, 143–149.

Arai, S., Miura, M., Tamura, A., Akizawa, N., Ishikawa, A., 2020. Hydrothermal chromitites from the Oman ophiolite: The role of water in chromitite genesis. Minerals 10(3).

Augé, T., 1987. Chromite deposits in the northern Oman ophiolite: Mineralogical constraints. Mineralium Deposita 22(1), 1–10.

Augé, T., Johan, Z., 1988. Comparative Study of Chromite Deposits from Troodos, Vourinos, North Oman and New Caledonia Ophiolites. In *Mineral Deposits within the European Community* (pp. 267–288).

Avcı, E., Uysal, İ., Akmaz, R. M., Saka, S., 2017. Ophiolitic chromitites from the Kızılyüksek area of the Pozantı-Karsantı ophiolite (Adana, southern Turkey): Implication for crystallization from a fractionated boninitic melt. Ore Geology Reviews 90, 166–183.

Barnes, S. J., Roeder, P. L., 2001. The range of spinel compositions in terrestrial mafic and ultramafic rocks. Journal of Petrology 42(12), 2279–2302.

Bockrath, C., Ballhaus, C., Holzheid, A., 2004a. Fractionation of the platinum-group elements during mantle melting. Science 305, 1951–1953.

Bockrath, C., Ballhaus, C., Holzheid, A., 2004b. Stabilities of laurite RuS_2 and monosulfide liquid solution at magmatic temperature. In Chemical Geology (pp. 265–271).

Borisova, A. Y., Ceuleneer, G., Kamenetsky, V. S., Arai, S., Béjina, F., Abily, B., … Pokrovski, G. S., 2012. A new view on the petrogenesis of the Oman ophiolite chromitites from microanalyses of chromite-hosted inclusions. Journal of Petrology 53(12), 2411–2440.

Bosi, F., Andreozzi, G. B., Ferrini, V., Lucchesi, S., 2004. Behavior of cation vacancy in kenotetrahedral Cr-spinels from Albanian eastern belt ophiolites. American Mineralogist 89(10), 1367–1373.

Brenan, J. M., Andrews, D., 2001. High-temperature stability of laurite and Ru-Os-Ir alloy and their role in PGE fractionation in mafic magmas: Erratum. Canadian Mineralogist 39(6), 1747–1748.

Burgath, K.-P., Krauss, U., Mohr, M., 2002. Chromium ores and platinum-group-element occurrences in Europe and Turkey: inventory, evaluation and possibilities. Chronique de la recherche minière, N o hors série, pp. 55–75.

Bussolesi, M., Grieco, G., Cavallo, A., Zaccarini, F., 2022. Different Tectonic Evolution of Fast Cooling Ophiolite Mantles Recorded by Olivine-Spinel Geothermometry: Case Studies from Iballe (Albania) and Nea Roda (Greece). Minerals 12(1).

Bussolesi, M., Grieco, G., Zaccarini, F., Cavallo, A., Tzamos, E., Storni, N., 2022. Chromite compositional variability and associated PGE enrichments in chromitites from the Gomati and Nea Roda ophiolite, Chalkidiki, Northern Greece. Mineralium Deposita 57, 1323-1342.

Cabri, L. J., Laflamme, J. H. G., Stewart, J. M., 1978. On cooperite, braggite, and vysotskite. American Mineralogist 63, 832–839.

Carbonin, S., Menegazzo, G., Lenaz, D., Princivalle, F., 1999. Crystal chemistry of two detrital Cr-spinels with unusually low values of oxygen positional parameter: Oxidation mechanisms and possible origin. Neues Jahrbuch Fur Mineralogie, Monatshefte, 359–371.

Carbonin, S., Russo, U., Della Giusta, A., 1996. Cation distribution in some natural spinels from X-ray diffraction and Mössbauer spectroscopy. Mineralogical Magazine 60(399), 355–368.

Chan, T.K., Finch, I.J., 2001. Determination of platinum-group elements and gold by inductively coupled plasma mass spectrometry. In: Australian Platinum Conference. Perth, Western Australia, pp. 1–9.

Chen, C., Su, B. X., Xiao, Y., Pang, K. N., Robinson, P. T., Uysal, I., … Kapsiotis, A., 2019. Intermediate chromitite in Kızıldağ ophiolite (SE Turkey) formed during subduction initiation in Neo-Tethys. Ore Geology Reviews 104, 88–100.

Corrivaux, L., Laflamme, J.H.G., 1990. Mineralogie des elements du groupe du platine dans les chromitites de l'ophiolite de Thetford Mines, Quebec. Canadian Mineralogist 28, 579–595.

Craig, J. R., 1971. VIOLARITE STABILITY RELATIONS. The American Mineralogist 56(7–8), 1303–1311.

De Grave, E., Van Alboom, A., 1991. Evaluation of ferrous and ferric Mössbauer fractions. Physics and Chemistry of Minerals 18(5), 337–342.

Derbyshire, E. J., O'Driscoll, B., Lenaz, D., Gertisser, R., Kronz, A., 2013. Compositionally heterogeneous podiform chromitite in the Shetland Ophiolite Complex (Scotland): Implications for chromitite petrogenesis and late-stage alteration in the upper mantle portion of a supra-subduction zone ophiolite. Lithos 162–163, 279–300.

Dick, H. J. B., 1977. Partial melting in the Josephine Peridotite; I, The effect on mineral composition and its consequence for geobarometry and geothermometry. American Journal of Science 277(7), 801–832.

Dmitrenko, G. G., Mochalov, A. G., 1989. Origin of hydrous silicate inclusions in PGM and Cr-spinels from ultramafic rocks. Doklady Akademii Nauk SSSR 307, 1207-1211.

Dönmez, C., Keskin, S., Günay, K., Çolakoğlu, A. O., Çiftçi, Y., Uysal, I., … Yildirim, N., 2014. Chromite and PGE geochemistry of the elekdağ ophiolite (kastamonu, northern turkey): Implications for deep magmatic processes in a supra-subduction zone setting. Ore Geology Reviews 57, 216–228.

Eeckhout, S. G., De Grave, E., 2003. Evaluation of ferrous and ferric Mössbauer fractions. Part II. Physics and Chemistry of Minerals, 30(3), 142–146.

Eslami, A., Malvoisin, B., Brunet, F., Kananian, A., Bach, W., Grieco, G., Cavllo, A., Gatta, G. D., 2021. Podiform magnetite ore(s) in the Sabzevar ophiolite (NE Iran): oceanic hydrothermal alteration of a chromite deposit. Contributions to Mineralogy and Petrology, 176(6).

Eslami, A., Malvoisin, B., Brunet, F., 2023. Hydrothermal alteration of chromitite-dunite pairs from the Sabzevar ophiolite (NE Iran): Chemical and nano-textural evolution of Cr-spinel. Lithos 442-443, 107093.

Faramarzi, R., Alikhani, M., Pourfaraj, H., Akhoundi, H., Mehrvarz, A., Sohrabi Mehr, M., Ansari, M., 2017. Geological Map of the Cheshmeh-Khan, KBC Exploration group, scale 1:25,000.

Faramarzi, R., Pourfaraj, H., Alikhani, M., Akhoundi, H., Mehrvarz, A., Sohrabi Mehr, M., Ansari, M., 2018. Geological Map of the Cheshmeh-Palangan, KBC Exploration group, scale 1:25,000.

Field, S. W., Haggerty, S. E., 1994. Symplectites in upper mantle peridotites: Development and implications for the growth of subsolidus garnet, pyroxene and spinel. Contributions to Mineralogy and Petrology 118(2), 138–156.

Förster, B., Braga, R., Aulbach, S., Lo Pò, D., Bargossi, G. M., Mair, V., 2017. A petrographic study of carbonate phases in the Ulten Zone ultramafic rocks: Insights into carbonation in the mantle wedge and exhumation-related decarbonation. Ofioliti 42(2), 105–127.

Franz, L., Wirth, R., 2000. Spinel inclusions in olivine of periodotite xenoliths from TUBAF seamount (Bismarck Archipelago/Papua New Guinea): Evidence for the thermal and tectonic evolution of the oceanic lithosphere. Contributions to Mineralogy and Petrology 140(3), 283–295.

Frost, B. R., 1985. On the stability of sulfides, oxides, and native metals in serpentinite. Journal of Petrology 26(1), 31–63.

Gale, A., Dalton, C. A., Langmuir, C. H., Su, Y., Schilling, J. G., 2013. The mean composition of ocean ridge basalts. Geochemistry, Geophysics, Geosystems 14(3), 489–518.

Garuti, G., Gazzotti, M., Torresruiz, J., 1995. Iridium, Rhodium, and Platinum Sulfides in Chromitites from the Ultramafic Massifs of Finero, Italy, and Ojen, Spain. Canadian Mineralogist 33, 509–520.

Garuti, G., Pushkarev, E. V., Thalhammer, O. A. R., Zaccarini, F., 2012. Chromitites of the urals (Part 1): Overview of chromite mineral chemistry and geo-tectonic setting. Ofioliti 37(1), 27-53.

Garuti, G., Zaccarini, F., 1997. In situ alteration of platinum-group minerals at low temperature: Evidence from serpentinized and weathered chromitite of the vourinos complex, Greece. Canadian Mineralogist 35(3), 611–626.

Gauthier, M., Corrivaux, L., Trottier, L. J., Cabri, J., Laflamme, J. H. G., Bergeron, M., 1990. Chromitites platinifères des complexes ophiolitiques de l'Estrie-Beauce, Appalaches du sud du Québec. Mineralium Deposita 25(3), 169–178.

Gervilla, F., Proenza, J. A., Frei, R., González-Jiménez, J. M., Garrido, C. J., Melgarejo, J. C., … Lavaut, W., 2005. Distribution of platinum-group elements and Os isotopes in chromite ores from Mayarí-Baracoa Ophiolitic Belt (eastern Cuba). Contributions to Mineralogy and Petrology 150(6), 589–607.

Ghiorso, M. S., Sack, R. O., 2019. Thermochemistry of the oxide minerals. In Oxide Minerals: Petrologic and Magnetic Significance (pp. 241–255).

Goble, R.J., Robinson, G., 1980. Geerite, Cu (sub 1.60) S, a new copper sulfide from Dekalb Township, New York. Canadian Mineralogist 18, 519–523.

Godard, G., Martin, S., 2000. Petrogenesis of kelyphites in garnet peridotites: A case study from the Ulten zone, Italian Alps. In Journal of Geodynamics (pp. 117–145).

Godard, M., Lagabrielle, Y., Alard, O., Harvey, J., 2008. Geochemistry of the highly depleted peridotites drilled at ODP Sites 1272 and 1274 (Fifteen-Twenty Fracture Zone, Mid-Atlantic Ridge): Implications for mantle dynamics beneath a slow spreading ridge. Earth and Planetary Science Letters 267(3–4), 410–425.

González-Jiménez, J. M., Kerestedjian, T., Proenza, J. A., Gervilla, F., 2009. Metamorphism on chromite ores from the Dobromirtsi Ultramafic Massif, Rhodope Mountains (SE Bulgaria). Geologica Acta 7(4), 413–429.

González-Jiménez, J. M., Proenza, J. A., Gervilla, F., Melgarejo, J. C., Blanco-Moreno, J. A., Ruiz-Sánchez, R., Griffin, W. L., 2011. High-Cr and high-Al chromitites from the Sagua de Tánamo district, Mayarí-Cristal ophiolitic massif (eastern Cuba): Constraints on their origin from mineralogy and geochemistry of chromian spinel and platinum-group elements. Lithos 125(1–2), 101–121.

González-Jiménez, J. M., Gervilla, F., Griffin, W. L., Proenza, J. A., Augé, T., O'Reilly, S. Y., Pearson, N. J., 2012. Os-isotope variability within sulfides from podiform chromitites. Chemical Geology 291, 224–235.

González-Jiménez, J. M., Augé, T., Gervilla, F., Bailly, L., Proenza, J. A., Griffin, W. L., 2011. Mineralogy and geochemistry of platinum-rich chromitites from the mantle-crust transition zone at Ouen Island, New Caledonia Ophiolite. Canadian Mineralogist 49(6), 1549–1569.

González-Jiménez, J. M., Gervilla, F., Kerestedjian, T., Proenza, J. A., 2010. Alteration of platinum-group and base-metal mineral assemblages in ophiolite chromitites from the dobromirtsi massif, Rhodope Mountains (Bulgaria). Resource Geology, 60(4), 315–334.

González-Jiménez, J. M., Griffin, W. L., Gervilla, F., Proenza, J. A., O'Reilly, S. Y., Pearson, N. J., 2014. Chromitites in ophiolites: How, where, when, why? Part I. A review and new ideas on the origin and significance of platinum-group minerals. Lithos 189, 127-139.

González-Jiménez, J. M., Mondal, S. K., Ghosh, B., Griffin, W. L., O'Reilly, S. Y., 2020. Re-os isotope systematics of sulfides in chromitites and host lherzolites of the andaman ophiolite, India. Minerals 10(8), 1–21.

González-Jiménez, J. M., Reich, M., 2017. An overview of the platinum-group element nanoparticles in mantle-hosted chromite deposits. Ore Geology Reviews 81, 1236-1248.

Greenbaum, D., 1977. The chromitiferous rocks of the Troodos ophiolite complex, Cyprus. Economic Geology 72(7), 1175–1194.

Grieco, G., Diella, V., Chaplygina, N. L., Savelieva, G. N., 2007. Platinum group elements zoning and mineralogy of chromitites from the cumulate sequence of the Nurali massif (Southern Urals, Russia). Ore Geology Reviews 30(3–4), 257–276.

Grieco, G., Bussolesi, M., Eslami, A., Gemile, A., Cavallo, A., Lian, D., … Ghaseminejad, F., 2020. Differential platinum group elements (PGE) re-mobilization at low fS2 in Abdasht and Soghan mafic-ultramafic complexes (Southern Iran). Lithos 366–367, 105523.

Günay, K., Çolakoğlu, A. R., 2016. Spinel compositions of mantle-hosted chromitite from the Eastern Anatolian ophiolite body, Turkey: Implications for deep and shallow magmatic processes. Ore Geology Reviews 73, 29–41.

Hewitt, R. L., 1938. Experiments bearing on the relation of pyrrhotite to other sulphides. Economic Geology 33(3), 305–338.

Hickey, R. L., Frey, F. A., 1982. Geochemical characteristics of boninite series volcanics: implications for their source. Geochimica et Cosmochimica Acta 46(11), 2099–2115.

Huang, J., Hao, J., Huang, F., Sverjensky, D. A., 2019. Mobility of chromium in high temperature crustal and upper mantle fluids. Geochemical Perspectives Letters 12, 1-6.

Hulbert, L. J., Von Gruenewaldt, G., 1985. Textural and compositional features of chromite in the lower and critical zones of the Bushveld complex south of Potgietersrus. Economic Geology 80(4), 872–895.

Irvine, T. N., 1977. Origin of chromitite layers in the Muskox intrusion and other stratiform intrusions: A new interpretation. Geology 5(5), 273–277.

Ismail, S. A., Kettanah, Y. A., Chalabi, S. N., Ahmed, A. H., Arai, S., 2014. Petrogenesis and PGE distribution in the Al- and Cr-rich chromitites of the Qalander ophiolite,

Journal Pre-proof

northeastern Iraq: Implications for the tectonic environment of the Iraqi Zagros Suture Zone. Lithos 202-203, 21-36.

Ismail, S. A., Mirza, T. M., Carr, P. F., 2010. Platinum-group elements geochemistry in podiform chromitites and associated peridotites of the Mawat ophiolite, northeastern Iraq. Journal of Asian Earth Sciences 37(1), 31–41.

Johan, Z., Dunlop, H., LeBel, L., Robert, J.L., Volfinger, M., 1983. Origin of chromite deposits
in ophiolitic complexes: evidence for a volatile and Na-rich reducing fluid. Fortschritte der Mineralogie 61, 105–107.

Johan, Z., 1986. Chromite deposits in the Massif du Sud ophiolite, New Caledonia: genetic considerations. In: Petraschek, W., Karamata, S., Kravchenko, G., Johan, Z., Economou, M., Engin, T. (Eds.), Metallogeny of Ophiolites, UNESCO IGCP 197 Project, pp. 311–339 (Theophrastus, Athens).

Johan, Z., Martin, R. F., Ettler, V., 2017. Fluids are bound to be involved in the formation of ophiolitic chromite deposits. European Journal of Mineralogy 29 (4), 543-555.

Kamenetsky, V. S., Crawford, A. J., Meffre, S., 2001. Factors controlling chemistry of magmatic spinel: An empirical study of associated olivine, Cr-spinel and melt inclusions from primitive rocks. Journal of Petrology 42, 655–671.

Kapsiotis, A., Grammatikopoulos, T. A., Tsikouras, B., Hatzipanagiotou, K., 2010. Platinum-group mineral characterization in concentrates from high-grade PGE Al-rich chromitites of korydallos area in the pindos ophiolite complex (NW Greece). Resource Geology 60(2), 178–191.

Kelemen, P. B., Shimizu, N., Salters, V. J. M., 1995. Extraction of mid-ocean-ridge basalt from the upwelling mantle by focused flow of melt in dunite channels. Nature 375, 747–753.

Khedr, M. Z., Arai, S., 2012. Petrology and geochemistry of prograde deserpentinized peridotites from Happo-O'ne, Japan: Evidence of element mobility during deserpentinization. Journal of Asian Earth Sciences 43(1), 150–163.

Khedr, M. Z., Arai, S., 2013. Origin of Neoproterozoic ophiolitic peridotites in south Eastern Desert, Egypt, constrained from primary mantle mineral chemistry. Mineralogy and Petrology 107(5).

Khedr, M. Z., Arai, S., 2016. Chemical variations of mineral inclusions in Neoproterozoic high-Cr chromitites from Egypt: Evidence of fluids during chromitite genesis. Lithos, 240-243, 309-326

Khedr, M. Z., Arai, S., 2017. Peridotite-chromitite complexes in the Eastern Desert of Egypt: Insight into Neoproterozoic sub-arc mantle processes. Gondwana Research 52, 59–79.

Khedr, M. Z., Takazawa, E., Hauzenberger, C., Tamura, A., Arai, S., Stern, R. J., El-Awady, A., 2022. Petrogenesis of arc-related serpentinized peridotites (Egypt): Insights into

Neoproterozoic mantle evolution beneath the Arabian-Nubian Shield. Journal of Asian Earth Sciences 226, 105078.

Klein, F., Bach, W., 2009. Fe-Ni-Co-O-S phase relations in peridotite-seawater interactions. Journal of Petrology 50, 37–59.

Kocks, H., Melcher, F., Meisel, T., Burgath, K. P., 2007. Diverse contributing sources to chromitite petrogenesis in the Shebenik Ophiolitic Complex, Albania: Evidence from new PGE- and Os-isotope data. Mineralogy and Petrology 91, 139–170.

Kullerud, G., Yund, R. A., 1962. The Ni-S system and related minerals. Journal of Petrology 3(1), 126–175.

Kullerud, G., 1963. Thermal stability of pentlandite.The Canadian Mineralogist 7(3), 353–366.

Kuo, L. C., Essene, E. J., 1986. Petrology of spinel harzburgite xenoliths from the Kishb Plateau, Saudi Arabia. Contributions to Mineralogy and Petrology 93, 335–346.

Kutyrev, A. V., Kamenetsky, V. S., Sidorov, E. G., Abersteiner, A., Chubarov, V. M., 2020. Silicate inclusions in isoferroplatinum: Constraints on the origin of platinum mineralization in podiform chromitites. Ore Geology Reviews, 119, 103367.

Lensch, G. Davoudzadeh, M., 1982. Ophiolites in Iran. Neues Jahrbuch für Geologie und Paläontologie– Monatshefte 5, 306–20

Leake, B. E., Woolley, A. R., Arps, C. E. S., Birch, W. D., Gilbert, M. C., Grice, J. D., … Youzhi, G., 1997. Nomenclature of amphiboles: Report of the subcommittee on amphiboles of the international mineralogical association, commission on new minerals and mineral names. American Mineralogist 61(405), 295–310.

Leblanc, M., 1991. Platinum-group elements and gold in ophiolitic complexes: distribution and fractionation from mantle to oceanic floor. Ophiolite Genesis and Evolution of the Oceanic Lithosphere. Proc. Conference, Muscat, 1990.

Legendre, O., Auge, T., 1986. Mineralogy of platinum-group mineral inclusions in chromitites from different ophiolitic complexes. Metallogeny of Basic and Ultrabasic Rocks.

Lenaz D., Kamenetsky V.S., Crawford A.J., Princivalle F. 2000: Melt inclusion in detrital spinel from the SE Alps (Italy-Slovenia): a new approach to provenance studies of sedimentary basins. Contribution to Mineralogy and Petrology 139, 748—758.

Lenaz, D., Andreozzi, G. B., Mitra, S., Bidyananda, M., Princivalle, F., 2004. Crystal chemical and 57Fe Mössbauer study of chromite from the Nuggihalli schist belt (India). Mineralogy and Petrology, 80, 45–57.

Lenaz, D., Adetunji, J., Rollinson, H., 2014. Determination of $Fe^{3+}/\Sigma Fe$ ratios in chrome spinels using a combined Mössbauer and single-crystal X-ray approach: Application to

chromitites from the mantle section of the Oman ophiolite. Contributions to Mineralogy and Petrology 167.

Lenaz, D., Andreozzi, G. B., Bidyananda, M., Princivalle, F., 2014. Oxidation degree of chromite from Indian ophiolites: A crystal chemical and 57Fe Mössbauer study. Periodico Di Mineralogia 83(2), 241–255.

Lenaz, D., Skogby, H., Logvinova, A. M., Sobolev, N. V., Princivalle, F., 2013. A micro-Mössbauer study of chromites included in diamond and other mantle-related rocks. Physics and Chemistry of Minerals 40, 671–679.

Lenaz, D., Skogby, H., Rigonat, N., Berger, J., 2018. Following the amphibolite to greenschist metamorphic path through the structural parameters of spinels from amsaga (Mauritania). Minerals 8(1), 27.

Li, X. P., Chen, H. K., Wang, Z. L., Wang, L. J., Yang, J. S., Robinson, P., 2015. Spinel peridotite, olivine websterite and the textural evolution of the Purang ophiolite complex, western Tibet. Journal of Asian Earth Sciences 110, 55–71.

Li, Z., Ping, J. Y., Jin, M. Z., Liu, M. L., 2002. Distribution of Fe^{2+} and Fe^{3+} and next-nearest neighbour effects in natural chromites: Comparison between results of QSD and Lorentzian doublet analysis. Physics and Chemistry of Minerals 29, 485–494.

Liu, X., Su, B. X., Xiao, Y., Chen, C., Uysal, I., Jing, J. J., … Asamoah Sakyi, P., 2019. Initial subduction of Neo-Tethyan ocean: Geochemical records in chromite and mineral inclusions in the Pozantı-Karsantı ophiolite, southern Turkey. Ore Geology Reviews 110, 102926.

Lorand, J. P., Ceuleneer, G., 1989. Silicate and base-metal sulfide inclusions in chromites from the Maqsad area (Oman ophiolite, Gulf of Oman): A model for entrapment. Lithos 22(3), 173–190.

Lughi, V., Lenaz, D., Bonifacio, A., Princivalle, F., Sergo, V., Parisi, F., 2020. A Raman spectroscopy study of the oxidation processes in synthetic chromite $FeCr_2O_4$. Ceramics International 46(18), 29382–29387.

Malitch, K. N., Melcher, F., Mühlhans, H., 2001. Palladium and gold mineralization in podiform chromitite at Kraubath, Austria. Mineralogy and Petrology 73, 247-277.

Mattioli, G. S., Wood, B. J., 1988. Magnetite activities across the $MgAl_2O_4$-Fe_3O_4 spinel join, with application to thermobarometric estimates of upper mantle oxygen fugacity. Contributions to Mineralogy and Petrology 98, 148–162.

Matveev, S., Ballhaus, C., 2002. Role of water in the origin of podiform chromitite deposits. Earth and Planetary Science Letters 203, 235–243.

McElduff, B., Stumpfl, E. F., 1991. The chromite deposits of the Troodos complex, cyprus - Evidence for the role of a fluid phase accompanying chromite formation. Mineralium Deposita 26, 307–318.

Journal Pre-proof

Melcher, F., Grum, W., Thalhammer, T. V., Thalhammer, O. A. R., 1999. The giant chromite deposits at Kempirsai, Urals: Constraints from trace element (PGE, REE) and isotope data. Mineralium Deposita 34, 250–272.

Melcher, F., Grum, W., Simon, G., Thalhammer, T. V., Stumpfl, E. F., 1997. Petrogenesis of the ophiolitic giant chromite deposits of Kempirsai, Kazakhstan: A study of solid and fluid inclusions in chromite. Journal of Petrology, 38(10), 1419–1458.

Mellini, M., Rumori, C., Viti, C., 2005. Hydrothermally reset magmatic spinels in retrograde serpentinites: Formation of "ferritchromit" rims and chlorite aureoles. Contributions to Mineralogy and Petrology 149, 266–275.

Merlini, A., Giovanni, G., Valeria, D., 2009. Ferritchromite and chromian-chlorite formation in mélange-hosted Kalkan chromitite (Southern Urals, Russia). American Mineralogist 94(10), 1459–1467.

Moghadam, H. S., Corfu, F., Chiaradia, M., Stern, R. J., Ghorbani, G., 2014. Sabzevar Ophiolite, NE Iran: Progress from embryonic oceanic lithosphere into magmatic arc constrained by new isotopic and geochemical data. Lithos 210–211, 224–241.

Moghadam, H.S., Arai, S., .Griffin, W.L., Khedr, M.Z., Saccani, E., Henry, H., O'Reilly, S.Y., Ghorbani, G., 2022. Geochemical variability among stratiform chromitites and ultramafic rocks from Western Makran, South Iran. Lithos 106591

Morishita, T., Arai, S., 2003. Evolution of spinel-pyroxene symplectite in spinel-lherzolites from the Horoman Complex, Japan. Contributions to Mineralogy and Petrology 144, 509–522.

Morishita, T., Tani, K., Shukuno, H., Hirigane, Y., Tamura, A., Kumagai, H., Hellebrand, E., 2011. Diversity of melt conduits in the Izu-Bonin-Mariana forearc mantle: Implications for the earliest stage of arc magmatism. Geology 39(4), 411–414.

Naldrett, A. J., Duke, J. M., 1980. Platinum metals in magmatic sulfide ores. Science 208(4451), 1417–1424.

Noghreyan, M., 1982. Evolution geochimique, mineralogique et structurale d'un edificeophiolitique singulier: le massif de Sabzevar (partie centrale), NE de l'Iran. TheseDoc. d'Etat, Universite de Nancy, France, p 239

Ohnenstetter, M., Karaj, N., Neziraj, A., Johan, Z., Cina, A., 1991. Le potentiel platinifere des ophiolites: mineralisations en elements du groupe du platine (PGE) dans les massifs de Tropoja et Bulqiza, Albanie. Comptes Rendus - Academie Des Sciences, Serie II.

Omrani, H., 2018. Island-arc and Active Continental Margin Adakites from the Sabzevar Zone, Iran. Petrology 26(1), 96–113.

Park, G., Park, J. W., Heo, C. H., Kim, J., 2022. Distribution of mantle-melt interaction zone: A petrological exploration tool for podiform chromitite deposits in the Kalaymyo ophiolite, Myanmar. Journal of Geochemical Exploration 232, 106878.

Journal Pre-proof

Payot, B. D., Arai, S., Tamayo, R. A., Yumul, G. P., 2013. Textural evidence for the chromite-oversaturated character of the melt involved in podiform chromitite formation. Resource Geology, 63(3), 313–319.

Pearce, J. A., Barker, P. F., Edwards, S. J., Parkinson, I. J., Leat, P. T., 2000. Geochemistry and tectonic significance of peridotites from the South Sandwich arc-basin system, South Atlantic. Contributions to Mineralogy and Petrology 139, 36–53.

Plechov, P. Y., Shcherbakov, V. D., Nekrylov, N. A., 2018. Extremely magnesian olivine in igneous rocks. Russian Geology and Geophysics 59(12), 1702–1717.

Prescher, C., McCammon, C., Dubrovinsky, L., 2012. MossA: A program for analyzing energy-domain Mössbauer spectra from conventional and synchrotron sources. Journal of Applied Crystallography, 45(2), 329–331.

Prichard, H. M., Barnes, S. J., Godel, B., Reddy, S. M., Vukmanovic, Z., Halfpenny, A., Neary, C.R., Fisher, P. C., 2015. The structure of and origin of nodular chromite from the Troodos ophiolite, Cyprus, revealed using high-resolution X-ray computed tomography and electron backscatter diffraction. Lithos 218–219, 87–98.

Prichard, H. M., Ixer, R. A., Lord, R. A., Maynard, J., Williams, N., 1994. Assemblages of platinum-group minerals and sulfides in silicate lithologies and chromite-rich rocks within the Shetland ophiolite. Canadian Mineralogist 32(2), 271–294.

Prichard, H. M., Barnes, S. J., Fisher, P. C., Pagé, P., Zientek, M. L., 2017. Laurite and associated PGM in the Stillwater chromitites: Implications for processes of formation, and comparisons with laurite in the Bushveld and ophiolitic chromitites. Canadian Mineralogist, *55*(1), 121–144.

Prichard, H. M., Lord, R. A., 1990. Platinum and Palladium in the Troodos ophiolite complex, Cyprus. Canadian Mineralogist 28, 607-617.

Proenza, J., Gervilla, F., Melgarejo, J., Vera, O., Alfonso, P., Fallick, A., 2001. Genesis of sulfide-rich chromite ores by the interaction between chromitite and pegmatitic olivine - norite dikes in the Potosí Mine (Moa-Baracoa ophiolitic massif, Eastern Cuba). Mineralium Deposita 36(7), 658–669.

Proenza, J., Gervilla, F., Melgarejo, J. C., Bodinier, J. L., 1999. Al- and Cr-rich chromitites from the Mayari-Baracoa ophiolitic belt (Eastern Cuba): Consequence of interaction between volatile-rich melts and peridotites in suprasubduction mantle. Economic Geology 94(4), 547–566.

Pushkarev, E. V., Kamenetsky, V. S., Morozova, A. V., Khiller, V. V., Glavatskykh, S. P., Rodemann, T., 2015. Ontogeny of ore Cr-spinel and composition of inclusions as indicators of the pneumatolytic–hydrothermal origin of PGM-bearing chromitites from Kondyor massif, the Aldan Shield. Geology of Ore Deposits 57(5), 352–380.

Quintiliani, M., 2005. ^{57}Fe Mössbauer spectroscopy analysis of spinels: Fe^{3+}/Fe^{tot} quantification accuracy and consequences on fo2 estimate. Periodico Di Mineralogia 74(2), 139–146.

Journal Pre-proof

Quintiliani, M., Andreozzi, G. B., Graziani, G., 2006. Fe^{2+} and Fe^{3+} quantification by different approaches and fo2 estimation for Albanian Cr-spinels. American Mineralogist 91(5–6), 907–916.

Rahmani, F., Noghreyan, M., Khalili, M., 2007. Geochemistry of sheeted dikes in the Nain ophiolite (Central Iran). Ofioliti 32, 119–129.

Rampone, E., Vissers, R. L. M., Poggio, M., Scambelluri, M., Zanetti, A., 2009. Melt migration and intrusion during exhumation of the alboran lithosphere: The tallante mantle xenolith record (Betic Cordillera, SE Spain). Journal of Petrology 51(1–2), 295–325.

Robinson, P. T., Trumbull, R. B., Schmitt, A., Yang, J. S., Li, J. W., Zhou, M. F., … Xiong, F., 2015. The origin and significance of crustal minerals in ophiolitic chromitites and peridotites. Gondwana Research 27(2), 486–506.

Rollinson, H., Adetunji, J., Yousif, A. A., Gismelseed, A. M., 2012. New Mössbauer measurements of $Fe^{3+}/\Sigma Fe$ in chromites from the mantle section of the Oman ophiolite: evidence for the oxidation of the sub-oceanic mantle. Mineralogical Magazine 76(3), 579–596.

Rollinson, H., 2008. The geochemistry of mantle chromitites from the northern part of the Oman ophiolite: Inferred parental melt compositions. Contributions to Mineralogy and Petrology 156, 273–288.

Rollinson, H., Adetunji, J., Lenaz, D., Szilas, K., 2017. Archaean chromitites show constant $Fe^{3+}/\Sigma Fe$ in Earth's asthenospheric mantle since 3.8 Ga. Lithos 282–283, 316–325.

Rollinson, H., Mameri, L., Barry, T., 2018. Polymineralic inclusions in mantle chromitites from the Oman ophiolite indicate a highly magnesian parental melt. Lithos 310-311, 381-391.

Rospabé, M., Ceuleneer, G., Granier, N., Arai, S., Borisova, A. Y., 2019. Multi-scale development of a stratiform chromite ore body at the base of the dunitic mantle-crust transition zone (Maqsad diapir, Oman ophiolite): The role of repeated melt and fluid influxes. Lithos 350-351, 105235.

Rossetti, F., Nasrabady, M., Vignaroli, G., Theye, T., Gerdes, A., Razavi, M. H., Vaziri, H. M., 2010. Early Cretaceous migmatitic mafic granulites from the Sabzevar range (NE Iran): Implications for the closure of the Mesozoic peri-Tethyan oceans in central Iran. Terra Nova 22(1), 26–34.

Satsukawa, T., Piazolo, S., González-Jiménez, J. M., Colás, V., Griffin, W. L., O'Reilly, S. Y., … Kerestedjian, T. N., 2015. Fluid-present deformation aids chemical modification of chromite: Insights from chromites from Golyamo Kamenyane, SE Bulgaria. Lithos 228–229, 78–89.

Schiano, P., Clocchiatti, R., Lorand, J. P., Massare, D., Deloule, E., Chaussidon, M., 1997. Primitive basaltic melts included in podiform chromites from the Oman Ophiolite. Earth and Planetary Science Letters 146(3–4), 489–497.

Journal Pre-proof

Sepidbar, F., Khedr, M. Z., Ghorbani, M. R., Palin, R. M., Xiao, Y., 2021. Petrogenesis of arc-related peridotite hosted chromitite deposits in Sikhoran-Soghan mantle section, South Iran: Evidence for proto-forearc spreading to boninitic stages. Ore Geology Reviews 136, 104256.

Seyler, M., Lorand, J. P., Dick, H. J. B., Drouin, M., 2007. Pervasive melt percolation reactions in ultra-depleted refractory harzburgites at the Mid-Atlantic Ridge, 15° 20′N: ODP Hole 1274A. Contributions to Mineralogy and Petrology 153(3), 303–319.

Shafaii Moghadam, H., Zaki Khedr, M., Arai, S., Stern, R. J., Ghorbani, G., Tamura, A., Ottley, C. J., 2015. Arc-related harzburgite-dunite-chromitite complexes in the mantle section of the Sabzevar ophiolite, Iran: A model for formation of podiform chromitites. Gondwana Research 27(2), 575–593.

Shojaat, B., Hassanipak, A. A., Mobasher, K., Ghazi, A. M., 2003. Petrology, geochemistry and tectonics of the Sabzevar ophiolite, North Central Iran. Journal of Asian Earth Sciences, 21(9), 1053–1067.

Singh, A. K., Devi, L. D., Singh, N. I., Subramanyam, K. S. V., Singh, R. K. B., Satyanarayanan, M., 2013. Platinum-group elements and gold distributions in peridotites and associated podiform chromitites of the Manipur Ophiolitic Complex, Indo-Myanmar Orogenic Belt, Northeast India. Chemie Der Erde 73(2), 147–161.

Sepidbar, F., Khedr, M.Z., Ghorbani, M.R., Palin, R.M., Xiao, Y., 2021. Petrogenesis of arc-related peridotite hosted chromitite deposits in Sikhoran-Soghan mantle section, South Iran: Evidence for proto-forearc spreading to boninitic stages. Ore Geology Reviews 136, 104256

Spandler, C., Mavrogenes, J., Arculus, R., 2005. Origin of chromitites in layered intrusions: Evidence from chromite-hosted melt inclusions from the Stillwater Complex. Geology 33, 893-896.

Stern, R. J., 2004. Subduction initiation: Spontaneous and induced. Earth and Planetary Science Letters 226(3–4), 275–292.

Su, B., Liu, X., Chen, C., Robinson, P. T., Xiao, Y., Zhou, M., … Zhang, P., 2021. A new model for chromitite formation in ophiolites: Fluid immiscibility. Science China Earth Sciences 64, 220–230.

Suhr, G., Kelemen, P., Paulick, H., 2008. Microstructures in Hole 1274A peridotites, ODP Leg 209, Mid-Atlantic Ridge: Tracking the fate of melts percolating in peridotite as the lithosphere is intercepted. Geochemistry, Geophysics, Geosystems 9(3).

Sun, Y., Sun, M., 2005. Nickel sulfide fire assay improved for pre-concentration of platinum group elements in geological samples: A practical means of ultra-trace analysis combined with inductively coupled plasma-mass spectrometry. Analyst 130(5), 664–669.

Talkington, R. W., Watkinson, D. H., Whittaker, P. J., Jones, P. C., 1984. Platinum-group minerals and other solid inclusions in chromite of ophiolitic complexes: Occurrence and

petrological significance. TMPM Tschermaks Mineralogische Und Petrographische Mitteilungen *32*, 285–301.

Tsoupas, G., Economou-Eliopoulos, M., 2021. Transformation of PGM in supra subduction zones: Geochemical and mineralogical constraints from the Veria (Greece) podiform chromitites. Geoscience Frontiers 12(2), 827–842.

Tzamos, E., Filippidis, A., Michailidis, K., Koroneos, A., Rassios, A., Grieco, G., Pedrotti, M., Stamoulis, K., 2017. Mineral chemistry and formation of awaruite and heazlewoodite in the Xerolivado chromite mine, Vourinos, Greece. Bulletin of the Geological Society of Greece 50(4), 2047.

Ullah, Z., Li, J. W., Robinson, P. T., Wu, W. W., Khan, A., Dac, N. X., Adam, M. M. A., 2020. Mineralogy and geochemistry of peridotites and chromitites in the Jijal Complex ophiolite along the Main Mantle Thrust (MMT or Indus Suture Zone) North Pakistan. Lithos 366–367, 105566.

Uysal, I., Akmaz, R. M., Kapsiotis, A., Demir, Y., Saka, S., Avci, E., Müller, D., 2015. Genesis and geodynamic significance of chromitites from the Orhaneli and Harmancik ophiolites (Bursa, NW Turkey) as evidenced by mineralogical and compositional data. Ore Geology Reviews 65(P1), 26–41.

Uysal, I., Kapsiotis, A., Akmaz, R. M., Saka, S., Seitz, H. M., 2018. The Guleman ophiolitic chromitites (SE Turkey) and their link to a compositionally evolving mantle source during subduction initiation. Ore Geology Reviews 93, 98–113.

Uysal, I., Tarkian, M., Sadiklar, M. B., Sen, C., 2007. Platinum-group-element geochemistry and mineralogy of ophiolitic chromitites from the Kop Mountains, northeastern Turkey. Canadian Mineralogist 45(2), 355–377.

Uysal, I., Tarkian, M., Sadiklar, M. B., Zaccarini, F., Meisel, T., Garuti, G., Heidrich, S., 2009. Petrology of Al- and Cr-rich ophiolitic chromitites from the Muğla, SW Turkey: Implications from composition of chromite, solid inclusions of platinum-group mineral, silicate, and base metal mineral, and Os-isotope geochemistry. Contributions to Mineralogy and Petrology 158(5), 659–674.

Uysal, I., Zaccarini, F., Burhan Sadiklar, M., Bernhardt, H. J., Bigi, S., Garuti, G., 2009. Occurrence of rare Ru-Fe-Os-Ir-oxide and associated Platinum-group minerals (PGM) in the chromitite of Muğla ophiolite, SW-Turkey. Neues Jahrbuch Fur Mineralogie, Abhandlungen 185 (3), 323 – 333.

Vannucci, R., Shimizu, N., Piccardo, G. B., Ottolini, L., Bottazzi, P., 1993. Distribution of trace elements during breakdown of mantle garnet: an example from Zabargad. Contributions to Mineralogy and Petrology 113(4), 437–449.

Velicogna, M., Lenaz, D., 2017. Is 600 °C enough to produce air oxidation in Cr-spinels? Neues Jahrbuch Fur Mineralogie, Abhandlungen 194(2), 125–137.

Watenphul, A., Schmidt, C., Jahn, S., 2014. Cr(III) solubility in aqueous fluids at high pressures and temperatures. Geochimica et Cosmochimica Acta 126, 212–227.

Whattam, S. A., Stern, R. J., 2011. The "subduction initiation rule": A key for linking ophiolites, intra-oceanic forearcs, and subduction initiation. Contributions to Mineralogy and Petrology 162, 1031–1045.

Whittaker, P. J., Watkinson, D. H., 1984. Genesis of chromitite from the Mitchell Range, Central British Columbia. Canadian Mineralogist 22, 161–172.

Xiong, F., Yang, J., Robinson, P. T., Gao, J., Chen, Y., Lai, S., 2017a. Petrology and geochemistry of peridotites and podiform chromitite in the Xigaze ophiolite, Tibet: Implications for a suprasubduction zone origin. Journal of Asian Earth Sciences 146, 56–75.

Xiong, Q., Henry, H., Griffin, W.L., Zheng, J-P., Satsukawa, T., Pearson, N.J., O'Reilly, S.Y., 2017b. High- and low-Cr chromitite and dunite in a Tibetan ophiolite: evolution from mature subduction system to incipient forearc in the Neo-Tethyan Ocean. Contribution to Mineralogy and Petrology 172, 45.

Xiong, F., Yang, J., Xu, X., Kapsiotis, A., Hao, X., Liu, Z., 2018. Compositional and isotopic heterogeneities in the Neo-Tethyan upper mantle recorded by coexisting Al-rich and Cr-rich chromitites in the Purang peridotite massif, SW Tibet (China). Journal of Asian Earth Sciences 159, 109–129.

Xiong, F., Zoheir, B., Robinson, P. T., Yang, J., Xu, X., Meng, F., 2020. Genesis of the Ray-Iz chromitite, Polar Urals: Inferences to mantle conditions and recycling processes. Lithos, 374–375, 105699.

Xu, Y., Chen, S., Parlak, O., Arai, S., Dönmez, C., Hong, J., 2020. Discovery of extremely high-Al podiform chromitites from the Lycian (Marmaris) ophiolite, SW Turkey: Implications for chromitite genesis. Ore Geology Reviews 127, 103817.

Zaccarini, F., Pushkarev, E. V., Fershtater, G. B., Garuti, G., 200). Composition and mineralogy of PGE-rich chromitites in the Nurali lherzolite-gabbro complex, Southern Urals, Russia. Canadian Mineralogist 42(2), 545–562.

Zaeimnia, F., Kananian, A., Arai, S., Mirmohammadi, M., Imamalipour, A., Khedr, M. Z., Abbou-Kebir, K., 2017. Mineral chemistry and petrogenesis of chromitites from the Khoy ophiolite complex, Northwestern Iran: Implications for aggregation of two ophiolites. Island Arc 26(6).

Zhang, P. F., Uysal, I., Zhou, M. F., Su, B. X., Avcı, E., 2016. Subduction initiation for the formation of high-Cr chromitites in the Kop ophiolite, NE Turkey. Lithos 260, 345–355.

Zhang, P. F., Zhou, M. F., Su, B. X., Uysal, I., Robinson, P. T., Avcı, E., He, Y. S., 2017. Iron isotopic fractionation and origin of chromitites in the paleo-Moho transition zone of the Kop ophiolite, NE Turkey. Lithos 268–271, 65–75.

Zhou, M. F., Robinson, P. T., Malpas, J., Edwards, S. J., Qi, L., 2005. REE and PGE geochemical constraints on the formation of dunites in the Luobusa ophiolite, Southern Tibet. Journal of Petrology 46(3), 615–639.

Zhou, M. F., Robinson, P. T., Su, B. X., Gao, J. F., Li, J. W., Yang, J. S., Malpas, J., 2014. Compositions of chromite, associated minerals, and parental magmas of podiform chromite deposits: The role of slab contamination of asthenospheric melts in suprasubduction zone environments. Gondwana Research 26 (1), 262-283.

Zhou, M. F., Sun, M., Keays, R. R., Kerrich, R. W., 1998. Controls on platinum-group elemental distributions of podiform chromitites: A case study of high-Cr and high-Al chromitites from Chinese orogenic belts. Geochimica et Cosmochimica Acta 62(4), 677–688.

Zhou, M.F., Robinson, P.T., Bai, W.J., 1994. Formation of podiform chromites by melt–rock Interaction in the upper mantle. Mineralium Deposita 29, 98–10

Figure Captions:

Fig. 1. (a) Distribution of Mesozoic ophiolites in Iran; (b) Simplified geological map of the Sabzevar–Forumad ophiolites (modified after Shafaii Moghadam et al., 2014); (c) Simplified geological map of the study area in the central part of Sabzevar ophiolite (derived from after Bahroudi and Omrani, 1999).

Fig. 2. Geological map of the study area in the Kuh-Siah peridotite massif modified from the 1:25,000 geological maps of Cheshmeh Khan (KBC Exploration group, 2017), Chesmeh Palangan (Faramarzi et al., 2018) and 1:1000 geological map of Kalchenari-2 and Kalchenari-3 (Kavandegan Sabzevar (2017). Location of the studied chromitite deposits is shown with white-filled circles.

Fig. 3. Field photos showing (a) a far view of Kalchenari-2 deposit with high-Al chromitite and Kalchenari-3 deposit with high-Cr chromitites; (b) an individual chromitite body hosted by thick dunite in the Ebrahim deposit; (c) a series of intermittent chromitite pods hosted by serpentinite in the Imam Hossein deposit; (d) a thin layer of deformed chromitite along the strike-slip fault.

Fig. 4. ^{57}Fe Mössbauer spectrum of chromite obtained at room temperature. Fitted absorption doublets assigned to Fe^{2+} are indicated in blue color and to Fe^{3+} in red color. Diamonds denotes measured spectrum, and black curve represents summed fitted spectrum. The spectrum for KA3-1C was obtained using a conventional setup, spectrum for SI-2C was obtaien using the point-source technique.

Journal Pre-proof

Fig. 5. Back Scattered Electron (BSE) images of (a) mylonitic texture in massive chromitite from the Main Sineh-Kar deposit; (b) crack-seal network filled with calcite. (c) spherical aggregates of garnet filling cracks of intensively mylonitized chromitite. (d) irregular accumulation of Cr-spinel in disseminated chromitite from Kermaniha Tunnel deposit. Abbreviation: Cc-calcite; Spl-spinel; Mgt-magnetite; Grt-garnet; Srp- serpentine

Fig. 6. Back Scattered Electron (BSE) images of (a-b) subhedral to euhedral Cr-spinel in dunite samples; (d-f) embayed and vermicular spinel associated with ortho- and clinopyroxenes in harzburgite sample. Abbreviation: Srp-Serpentine; Cpx-Clinopyroxene; Opx-Orthopyroxene; Spl-Spinel.

Fig. 7. Back-scattered-electron (BSE) images showing the morphology and texture Cr-spinel-hosted silicate inclusions: (a) euhedral clinopyroxene partially altered to serpentine; (b-c) euhedral orthopyroxene; (d) rhombic amphibole; (e) alteration of Cr-spinel to Fe-rich Cr-spinel associated with garnet and serpentine. (f) serpentine inclusions scattered in highly deformed Cr-spinel grains; Abbreviations: Cpx-Clinopyroxene; Opx-Orthopyroxene; Srp-Serpentine; Amp-Amphibole; Grt-garnet; Fe-Chr-Ferrian Cr-spinel; Chl-Chlorite

Fig. 8. Back Scattered Electron (BSE) images of a) Ni-Fe alloy in massive chromitite sample SI-2C, b) chalcocite crystal in serpentinized dunite sample KE-3, c) detail of two polyphasic grains in sample IM-1B. d) sulfide trails enclosed in Cr-spinel in sample IM-1B, e) pentlandite crystal enclosed in unaltered Cr-spinel (KA-1B), f) chalcopyrite-millerite polyphasic grain in Cr-spinel of sample KA3-1C, g) Ni-Fe alloy and Co-Ni-Fe sulfide interstitial to Cr-spinel in sample KA3-1C, h) heazlewoodite crystal associated with an unknown silicate in unaltered Cr-spinel (KA5-1A), i) millerite and chalcopyrite polyphasic grain associated to clinopyroxene within Cr-spinel of sample HA21, j) polyphasic millerite, malanite, braggite, laurite, (BM,PGE)S grain within unaltered Cr-spinel of sample HA21, k) laurite crystal associated with amphibole, l) euhedral millerite included within Cr-spinel. m) laurite crystal in sample RO1B and n) a partially desulfurized pentlandite crystal enclosed in a ferrian-chromitized rim. (o) Ir-Rh-As sulfide (irarsite) surrounded by Ni-Fe alloy.

Fig. 9. (a-b) Compositional variations of Cr# (100*Cr/(Cr + Al)) versus Fe^{2+}# (100*Fe^{2+}/ (Fe^{2+} + Mg)) in Cr-spinels of the Kuh-Siah chromitite (a) and associated dunite (b). Chromitite, dunite and harzburgite are shown with circle, diamond and square, respectively.

(c) Compositional variations of Cr# (100*Cr/(Cr + Al)) versus Mg# (100*Mg / (Fe^{2+} + Mg)) in Cr-spinels of the Kuh-Siah chromitite and associated dunite. Compositional fields of spinel from mid-ocean ridge basalt (MORB) and boninite (BON) are from Barnes and Roeder (2001). The spinel-olivine re-equilibration curves (spin-oliv) at 1220°C from Dick (1977) are shown for comparison. Data of podiform chromitite from a suprasubduction zone (SSZ) nodular-textured chromitite xenolith from the Japan arc (Arai and Abe, 1994) is shown for comparison.

Fig. 10. (a) TiO_2 (wt. %) vs. Al_2O_3 (wt. %) plot of Cr-spinel from the Kuh-Siah chromitite bodies and associated peridotites. ARC, LIP, MORB and OIB compositional fields are from Kamenetsky et al. (2001), BABB compositional field is from Lenaz et al. (2000). Abbreviations: BABB – back-arc basin basalts, LIP – large igneous province (basalts), OIB – ocean islands basalts, MORB – mid-ocean ridge basalts. The two horizontal lines in the ARC field discriminate between the lower-Ti (boninites and tholeiites) and the higher-Ti (calc-alkaline and high-K) island-arc series. (b) Cr# versus TiO_2 (wt. %) plot of Cr-spinel in the studied samples. Abbreviations: BON – boninite series, IAT – island arc tholeiites. The diagram discriminates between partial melting trends and melt-rock reaction as modelled by Pearce et al., 2000. Subscripts; m - MORB, i– island arc tholeiite and b - boninite refer to the chemistries of the arc-basin lava Cr-spinel reference. IBM refers to the Izu-Bonin-Mariana system. The FMM partial melting curve illustrates the theoretical partial melting of fertile MORB mantle.

Fig. 11. (a) Chemical classification of the calcic amphibole inclusions (after Leake et al. (1997). (b) Pyroxene ternary diagram showing clino- and orthopyroxene inclusions hosted by Cr-spinel.

Fig. 12. (a) Mantle-normalized ratios of total PGE versus Pt/Ir for chromitites and associated dunite. Group definition based on Burgath et al. (2002); (b) Normalised Pd/Ir versus normalized Pt/Ir. (c) Cr# versus bulk PGE content in Cr-rich and Al-rich chromitites and associated dunites of the Kuh-Siah massif. (d) Pd/Ir vs. Pt/Pt* diagram for the Kuh-Siah chromitites and associated dunites. Average composition of the asthenosphere as well as fractionation and partial melting trends are from Garuti et al. (1997). The platinum (Pt) anomaly is calculated as follows: Pt/Pt* $Pt_n/(Rh_n \times Pd_n)^{½}$.

Journal Pre-proof

Fig. 13. Chondrite normalized (Naldrett and Duke, 1980) PGE patterns of high-Cr (a), high-Al chromitites (b) and associated dunite envelope (c) from the Kuh-Siah massif. Brown field is compilation of data from Proenza et al. (1999), Gervilla et al. (2005), Singh et al. (2013), Prichard and Lord (1990), Kocks et al. (2007), Ismail et al. (2014), Melcher et al. (1999), Chen et al. (2020), Ullah et al. (2020), Aldanmez et al. (2012), Xiong et al. (2017a), Ismail et al. (2010), Xiong et al. (2020) and Zhou et al. (2005). Blue fields are compilation of data from Xiong et al. (2018), Akmaz et al. (2014), Singh et al. (2013), Gonzalez-Jimenez et al. (2011), Xu et al. (2020), Donmenz et al. (2014), Gervilla et al. (2005), Ismail et al. (2014), Xiong et al. (2020), Ismail et al. (2010), Xiong et al. (2017a), Uysal et al. (2015), Günay and Çolakoğlu (2016), Ullah et al. (2020), Avci et al. (2017), Tsoupas and Economou et al. (2020), Uysal et al. (2018), Uysal et al. (2007) and Kapsiotis et al. (2010).

Fig. 14. EPMA vs. Mössbauer $Fe^{3+}/\Sigma Fe$ values. Red circles: Cr-spinels from the Kuh-Siah massif (conventional MS; this study); red squares: Cr-spinels from KE-2 and SI-2c samples from the Kuh-Siah massif (point source-MS; this study); black circles: Cr-spinels from Albania, Oman, India and Norway ophiolites (Quintiliani et al., 2006; Rollinson et al., 2012; Lenaz et al., 2014a, 2014b; O'Driscoll et al., 2021); grey circles: Cr-spinels from metamorphosed Archean rocks from Mauretania (Lenaz et al., 2018); white circles: Cr-spinels from Bushveld layered complex (Adetunjii et al., 2013; Langa et al., 2021). Black dotted line represents the 1:1 line. Red dashed lines connect the point source - MS analyses with the corresponding conventional - MS analyses.

Fig. 15. Ternary diagram (at %) of a) Fe-Ni Base Metal Minerals and b) Cu-Ni Base Metal Minerals within the Kuh-Siah chromitites and host rocks. Symbol colors as in Fig. 9.

Fig. 16. Ternary diagram (at.%) of A) minerals of the laurite-erlichmanite series and B) BM-PGE sulfides within the Kuh-Siah chromitites. Symbol colors as in Fig. 9.

Fig. 17. Schematic geodynamic diagram depicting the tectonomagmatic evolution of the NSOB in NE Iran and genesis of associated high-Al and high-Cr chromitites in an extended intra-oceanic arc–forearc SSZ setting between the Turan and Central Iran continental blocks in the mid to late Cretaceous.

Table Captions:

Journal Pre-proof

Table 1. General characteristics of studied chromitite deposits and associated peridotites in the Kuh-Siah massif. BBM: Base metal mineral, PGM: Platinum group mineral, Cr#: [(Cr/Cr + Al) × 100]

Supplementary Table Captions:

Table S1. Representative analyses of spinels from the Kuh-Siah chromitites and associated peridotites.

Table S2. Representative analyses of silicates of the Kuh-Siah chromitites and associated peridotites.

Table S3. Selected PGM and BMM analyses from chromitites and associated peridotites in the Kuh-Siah massif.

Table S4. Whole-rock PGE concentrations (ppb) in the Kuh-Siah chromitites and associated dunites.

Table S5. Mössbauer parameters for the Kuh-Siah chromitites measured at room-temperature.

Journal Pre-proof

Table 1. General characteristics of studied chromitite deposits and associated peridotites in the Sabzevar ophiolite belt. BBM: Base metal mineral, PGM: Platinum group mineral, Cr#: [(Cr/Cr + Al) × 100]

Mine	North	East	Sample	Rock type	Microstructure	BMM	PGM	Cr# Spinel	TiO_2 Spinel (wt%)
Imam-Hossein	36°25'39.39"	57°18'31.31"	IM-1B	Chromitite	Massive	Geerite, Polydymite		69-77	0.08-0.30
			IM-2	Serpentinized dunite		Awaruite		54-61	
			IM-3A	Harzburgite				49-53	
Main Sineh-Kar	36°25'47.74"	57°17'50.99"	SI-2C	Chromitite	Semi-massive	Awaruite		61-62	0.05-0.12
			SI-2B	Serpentinized dunite				78-79	
Kermaniha Tunnel	36°25'47.53"	57°17'45.80"	KE-2	Chromitite	Semi-massive			70-71	0.14-0.20
			KE-3	Serpentinized dunite		Chalcocite		71-73	
Kalchenari 1	36°26'59.20"	57°20'56.80"	KA1-1B	Chromitite	Semi-massive	Pentlandite		64	0.15-0.18
			KA1-1A	Serpentinized dunite				62-64	
Kalchenari 2	36°26'18.17"	57°20'56.12"	F1	Chromitite	Massive	Awaruite	Ir-Rh-As sulfide (irarsite)	50-54	0.09-0.15
			F3	Serpentinized dunite				52-53	
			F2	Harzburgite				55-59	
Kalchenari 3	36°26'18.17"	57°20'56.12"	KA3-1C	Chromitite	Semi-massive (nodular)	Co-pentlandite, millerite, chalcopyrite, Awaruite		65-66	0.17-0.27
			KA3-5	Serpentinized dunite				62-67	
			KA3-3	Harzburgite				58-62	
Kalchenari 5	36°26'25.97"	57°20'24.83"	KA5-1A	Chromitite	Disseminated	Heazlewoodite		66	0.19-0.25
Ebrahim	36°25'40.11"	57°20'12.47"	EB-2	Chromitite	Massive	Awaruite	Laurite	X	
			EB-3	Serpentinized dunite				70-73	
			EB-4	Chromitite	Massive	Millerite	Laurite	71-73	0.08-0.17
			EB-5A	Serpentinized dunite				63-65	
			[illegible]	Chromitite	Massive			66-68	0.06-0.17
			[illegible]	Chromitite	Massive			68-69	0.10-0.23
			[illegible]	Chromitite	Massive			71-72	0.08-0.17
Haj-Ghasem	36°27'04.59"	57°21'17.43"	HA2-1	Chromitite	Semi-massive	Millerite, Bornite, Awaruite	Laurite, Malanite, Braggite, (BM,PGE)S	73-74	0.09-0.22
			HA2-2A	Serpentinized dunite				68-73	
Roholla New	36°25'19.91"	57°19'20.98"	RO-1B	Chromitite	Massive	Pentlandite	Laurite	63-68	0.06-0.19
			RO-2A	Serpentinized dunite				70-72	

Journal Pre-proof

Declaration of interests

☐The authors declare that they have no known competing financial interests or personal relationships that could have appeared to influence the work reported in this paper.

☒The authors declare the following financial interests/personal relationships which may be considered as potential competing interests:

Alireza Eslami reports financial support was provided by University Grenoble Alpes. Alireza Eslami reports a relationship with University Grenoble Alpes that includes: funding grants.

Journal Pre-proof

Highlights

- Mineral chemistry and platinum group element (PGE) bulk-analyses of podiform chromitite deposits in the Sabzevar ophiolite, NE Iran.

-Co-occurrence of high-Cr and high-Al chromitites in the same massif and a single tectono-magmatic setting shared similar texture on outcrop scale to centimeter-millimeter scale

- Origin of PGM-bearing compositionally variable chromitites crystallized from different parent melts during the variable mantle oxidation state.

- Implications of solid inclusions and Platinum group minerals (PGM) for genesis of the Sabzevar spinels and host chromitites

-Localized post-magmatic oxidation linked to dominant hydrous fluids existing in the shear zone.

Journal Pre-proof

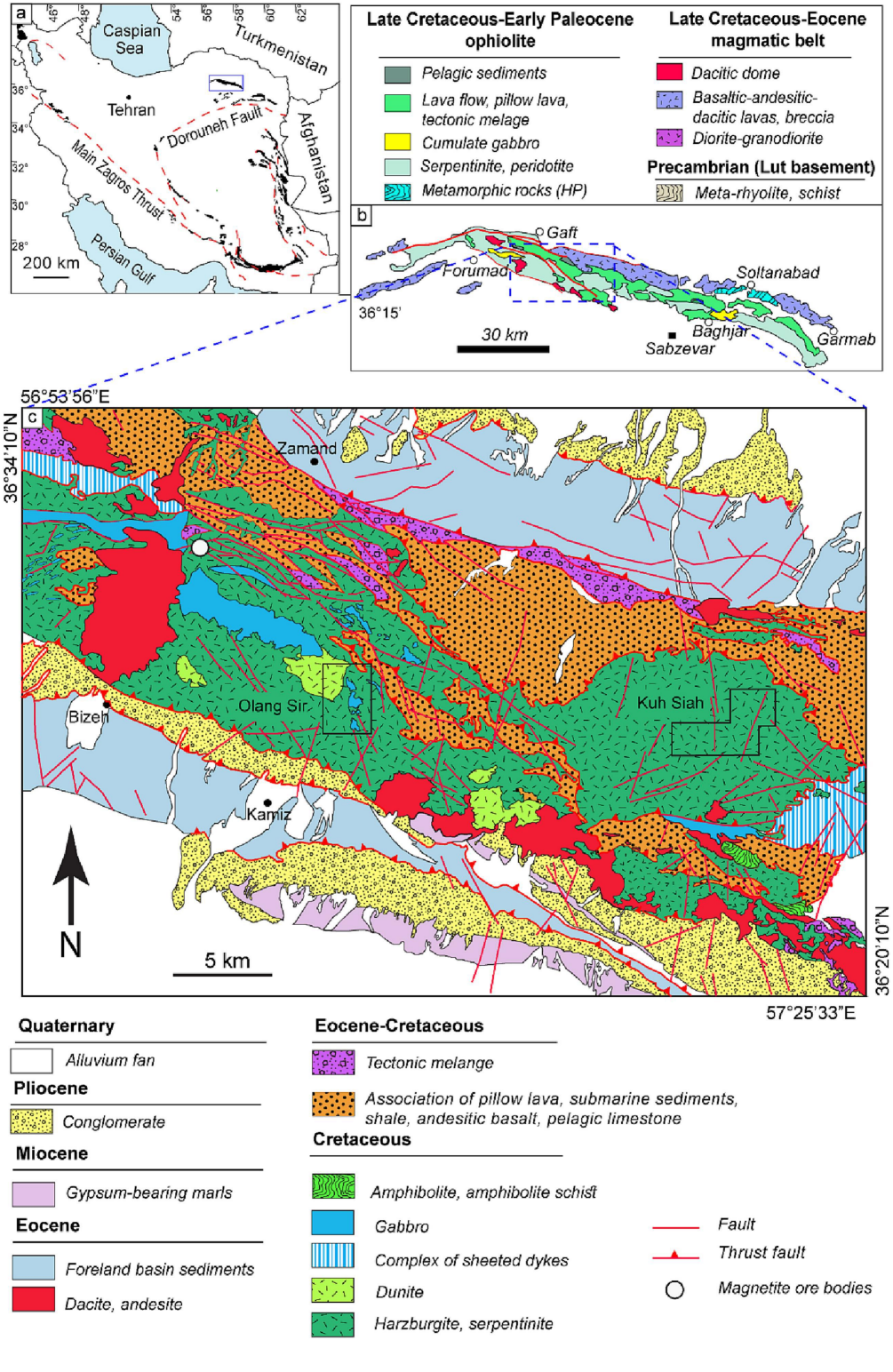
a
Caspian Sea
Turkmenistan
Tehran
Dorouneh Fault
Afghanistan
Main Zagros Thrust
Persian Gulf
200 km
Late Cretaceous-Early Paleocene ophiolite
Pelagic sediments
Lava flow, pillow lava, tectonic melage
Cumulate gabbro
Serpentinite, peridotite
Metamorphic rocks (HP)
Late Cretaceous-Eocene magmatic belt
Dacitic dome
Basaltic-andesitic-dacitic lavas, breccia
Diorite-granodiorite
Precambrian (Lut basement)
Meta-rhyolite, schist
b
Gaft
Forumad
Soltanabad
36°15'
30 km
Baghjar
Sabzevar
Garmab
56°53'56"E
c
36°34'10"N
Zamand
Olang Sir
Kuh Siah
Bizeh
Kamiz
N
5 km
36°20'10"N
57°25'33"E
Quaternary
Alluvium fan
Pliocene
Conglomerate
Miocene
Gypsum-bearing marls
Eocene
Foreland basin sediments
Dacite, andesite
Eocene-Cretaceous
Tectonic melange
Association of pillow lava, submarine sediments, shale, andesitic basalt, pelagic limestone
Cretaceous
Amphibolite, amphibolite schist
Gabbro
Complex of sheeted dykes
Dunite
Harzburgite, serpentinite
Fault
Thrust fault
Magnetite ore bodies

Figure 1

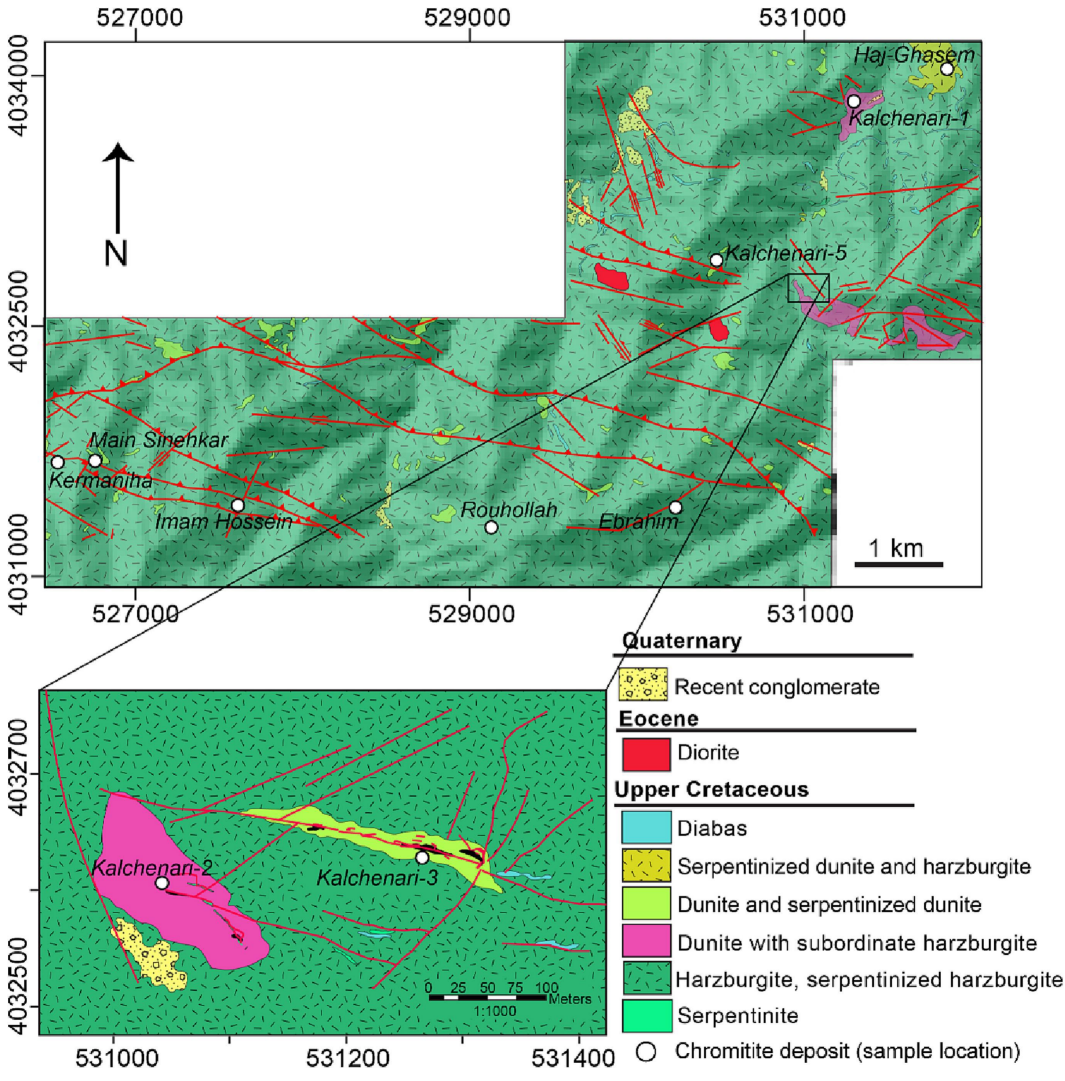
527000
529000
531000
4034000
4032500
4031000
N
Haj-Ghasem
Kalchenari-1
Kalchenari-5
Main Sinehkar
Kermanjha
Imam Hossein
Rouhollah
Ebrahim
1 km
4032700
4032500
Kalchenari-2
Kalchenari-3
0 25 50 75 100 Meters
1:1000
531000
531200
531400
Quaternary
Recent conglomerate
Eocene
Diorite
Upper Cretaceous
Diabas
Serpentinized dunite and harzburgite
Dunite and serpentinized dunite
Dunite with subordinate harzburgite
Harzburgite, serpentinized harzburgite
Serpentinite
Chromitite deposit (sample location)

Figure 2

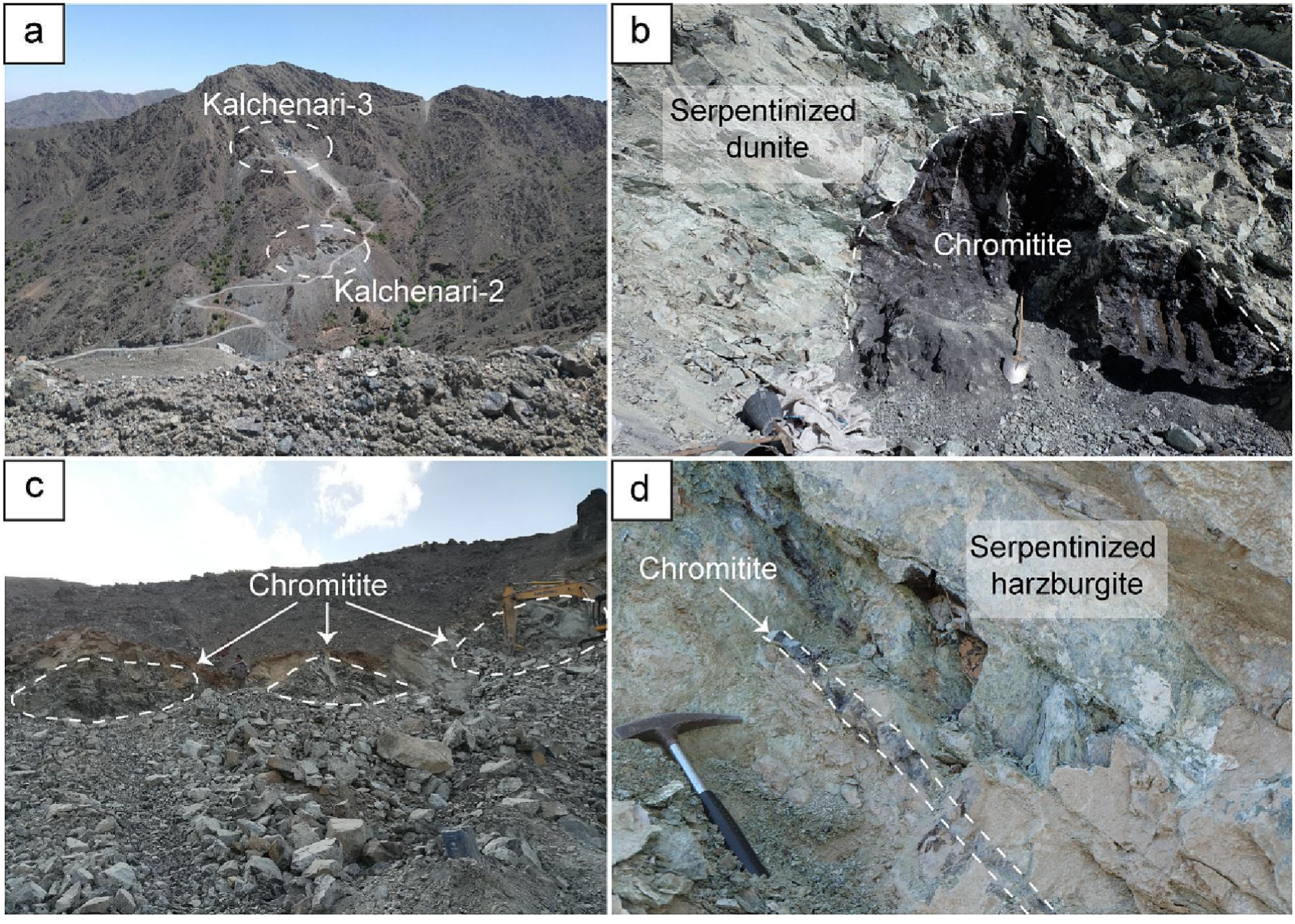
a
Kalchenari-3
Kalchenari-2
b
Serpentinized
dunite
Chromitite
c
Chromitite
d
Chromitite
Serpentinized
harzburgite

Figure 3

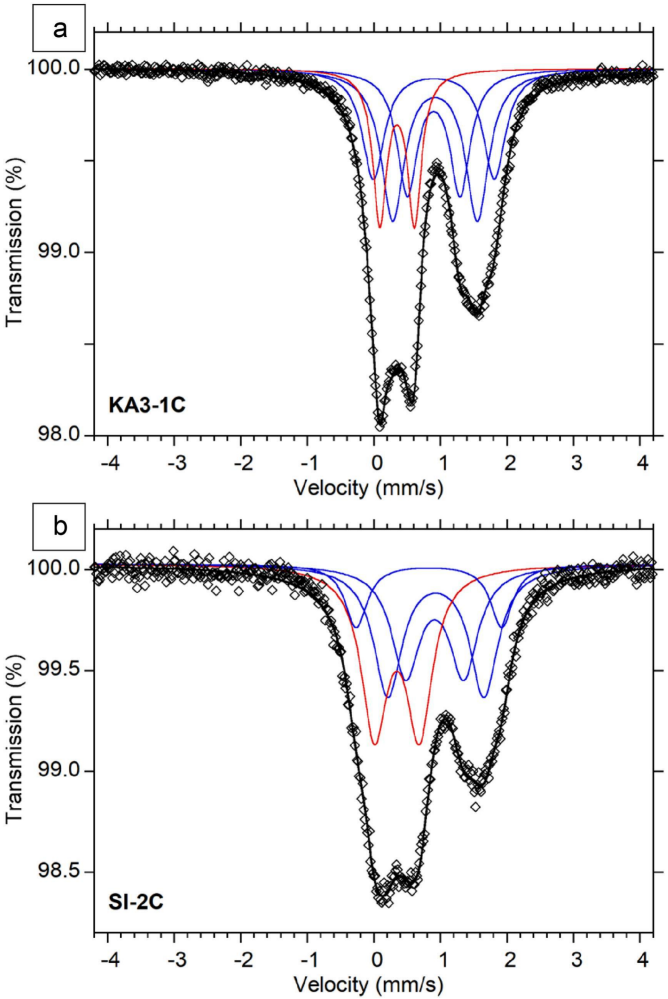
a
100.0
99.0
98.0
Transmission (%)
KA3-1C
-4
-3
-2
-1
0
1
2
3
4
Velocity (mm/s)
b
100.0
99.5
99.0
98.5
Transmission (%)
SI-2C
-4
-3
-2
-1
0
1
2
3
4
Velocity (mm/s)

Figure 4

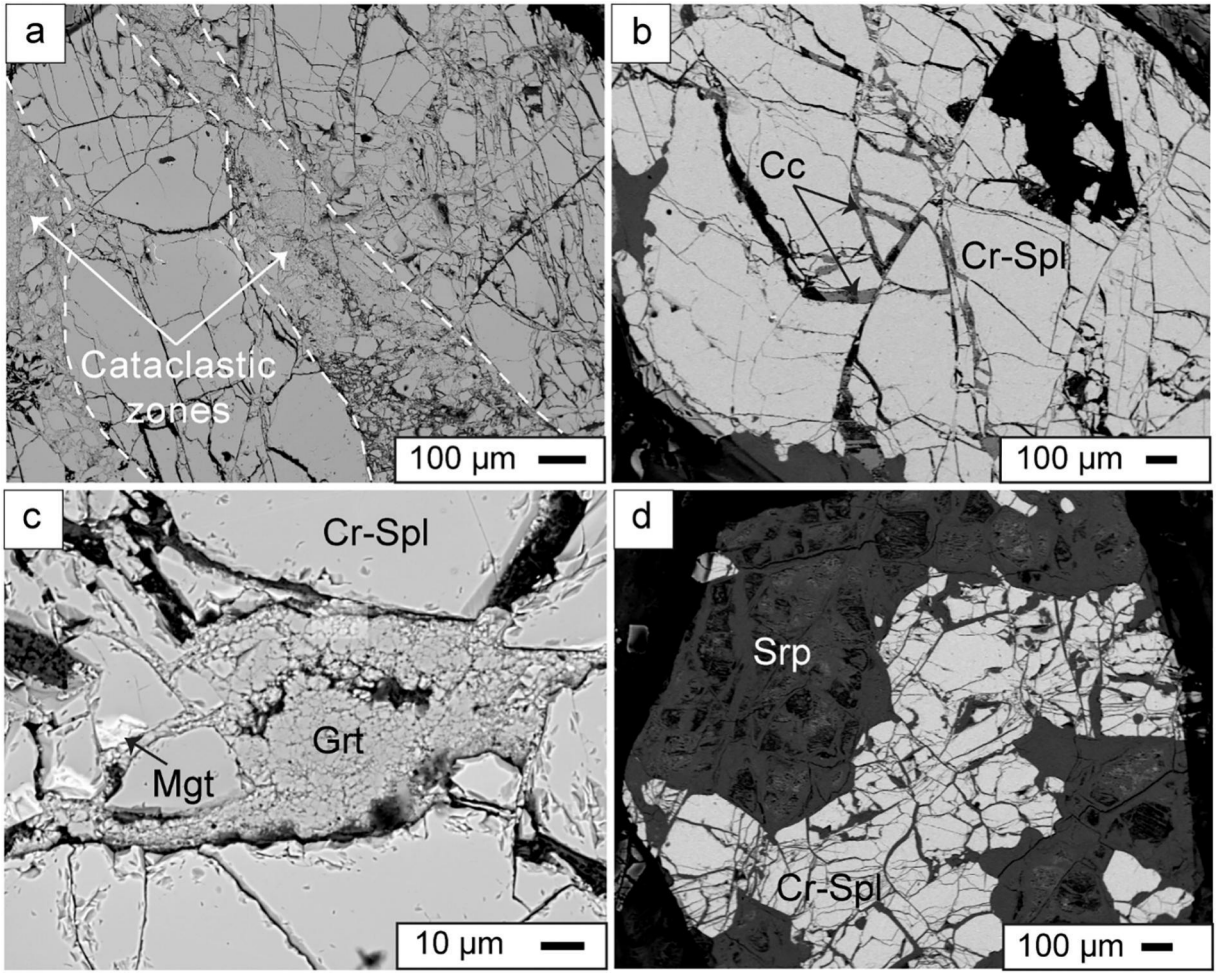
a
Cataclastic zones
100 µm
b
Cc
Cr-Spl
100 µm
c
Cr-Spl
Grt
Mgt
10 µm
d
Srp
Cr-Spl
100 µm

Figure 5

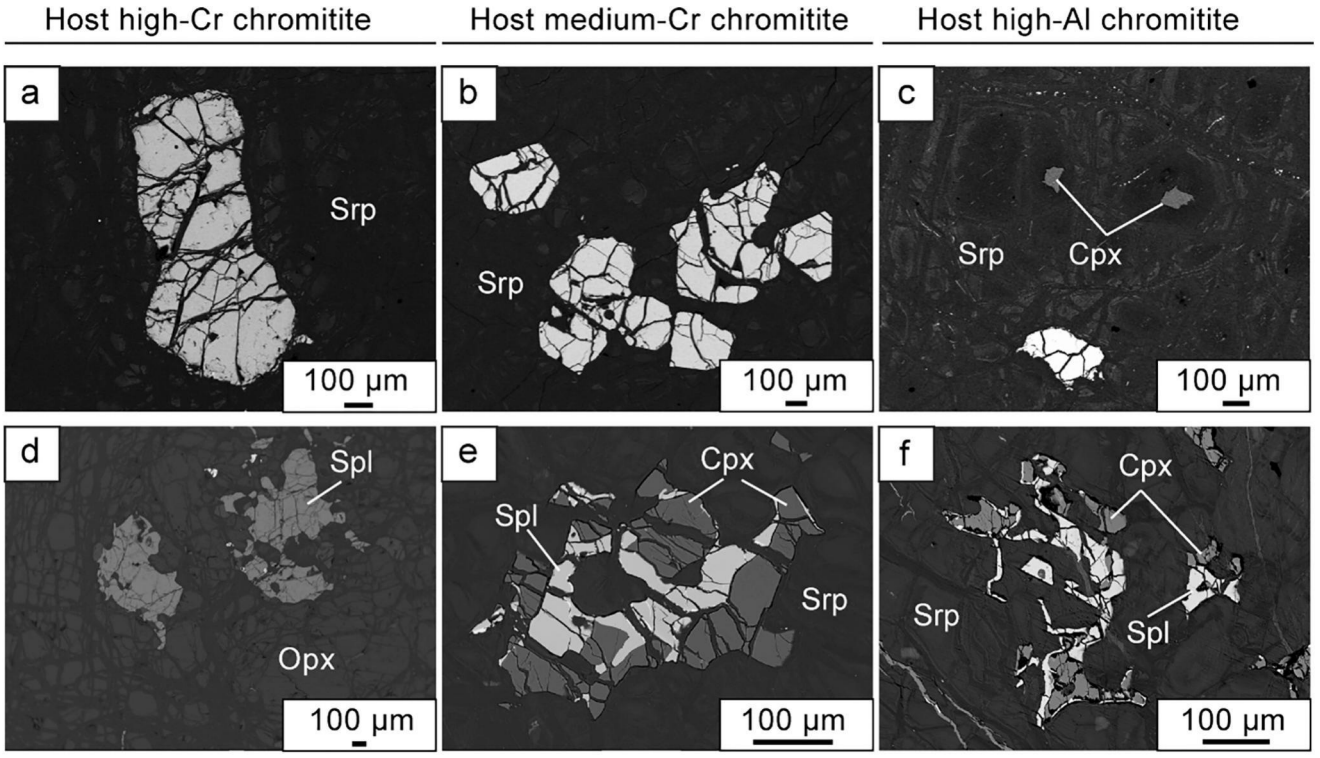
Host high-Cr chromitite
Host medium-Cr chromitite
Host high-Al chromitite
Dunite
Harzburgite
a
Srp
100 μm
b
Srp
100 μm
c
Srp
Cpx
100 μm
d
Spl
Opx
100 μm
e
Cpx
Spl
Srp
100 μm
f
Cpx
Srp
Spl
100 μm

Figure 6

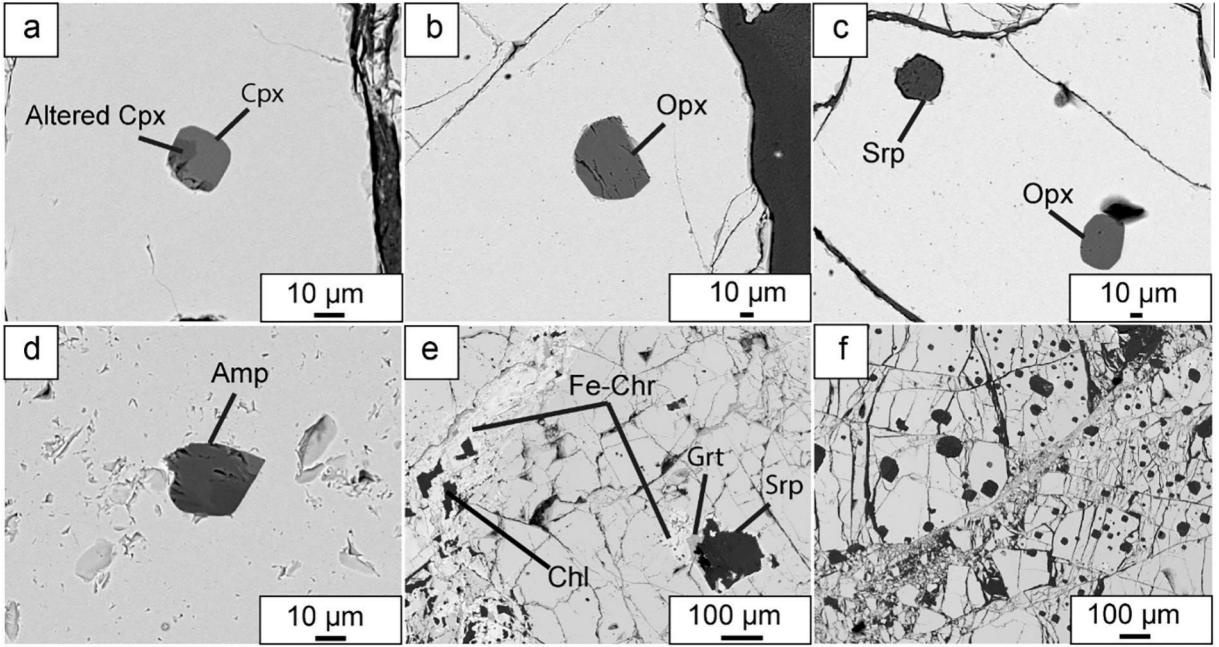
a
Altered Cpx
Cpx
10 µm
b
Opx
10 µm
c
Srp
Opx
10 µm
d
Amp
10 µm
e
Fe-Chr
Grt
Srp
Chl
100 µm
f
100 µm

Figure 7

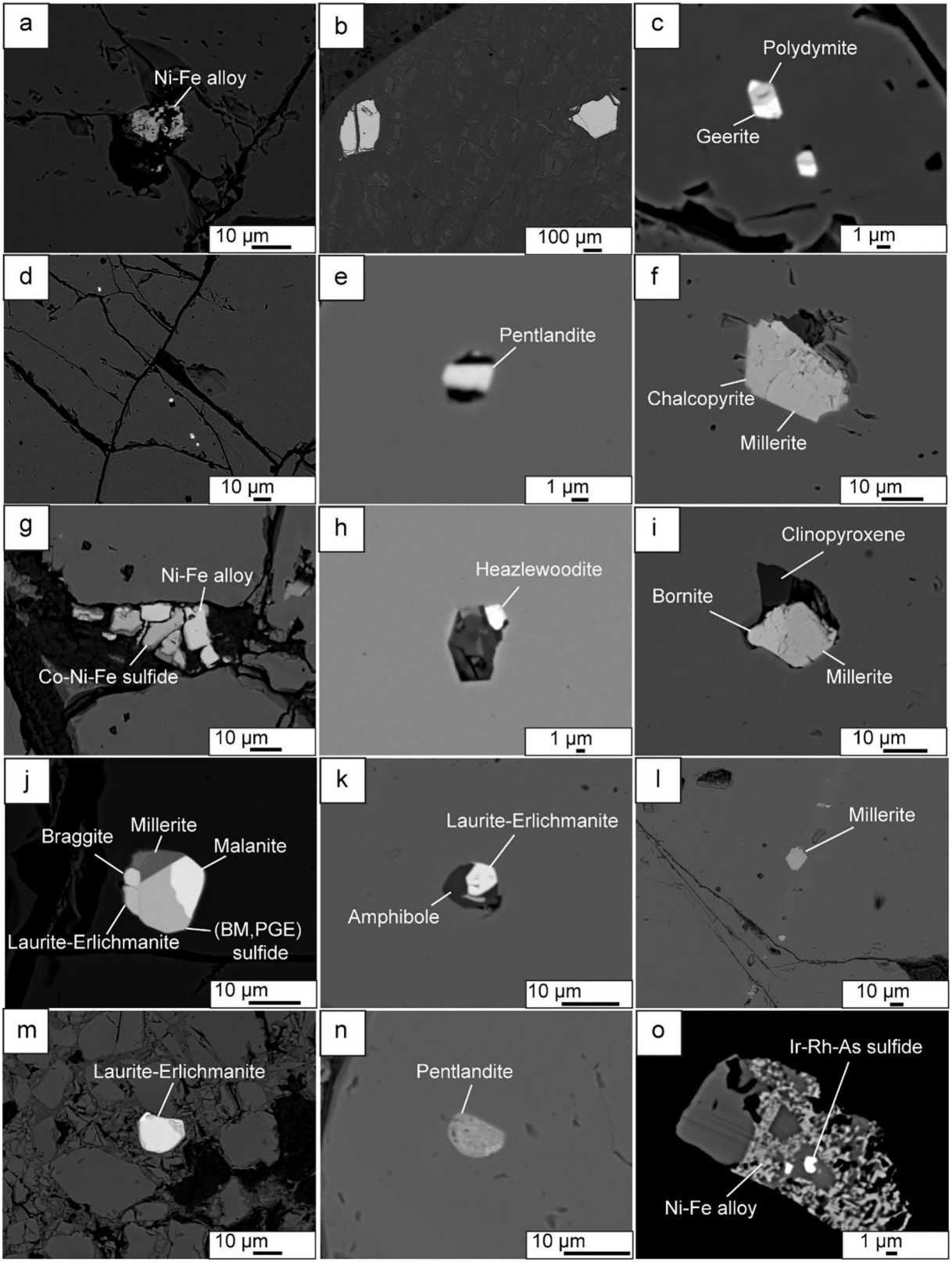
a
Ni-Fe alloy
10 μm
b
100 μm
c
Polydymite
Geerite
1 μm
d
10 μm
e
Pentlandite
1 μm
f
Chalcopyrite
Millerite
10 μm
g
Ni-Fe alloy
Co-Ni-Fe sulfide
10 μm
h
Heazlewoodite
1 μm
i
Clinopyroxene
Bornite
Millerite
10 μm
j
Braggite
Millerite
Malanite
Laurite-Erlichmanite
(BM,PGE) sulfide
10 μm
k
Laurite-Erlichmanite
Amphibole
10 μm
l
Millerite
10 μm
m
Laurite-Erlichmanite
10 μm
n
Pentlandite
10 μm
o
Ir-Rh-As sulfide
Ni-Fe alloy
1 μm

Figure 8

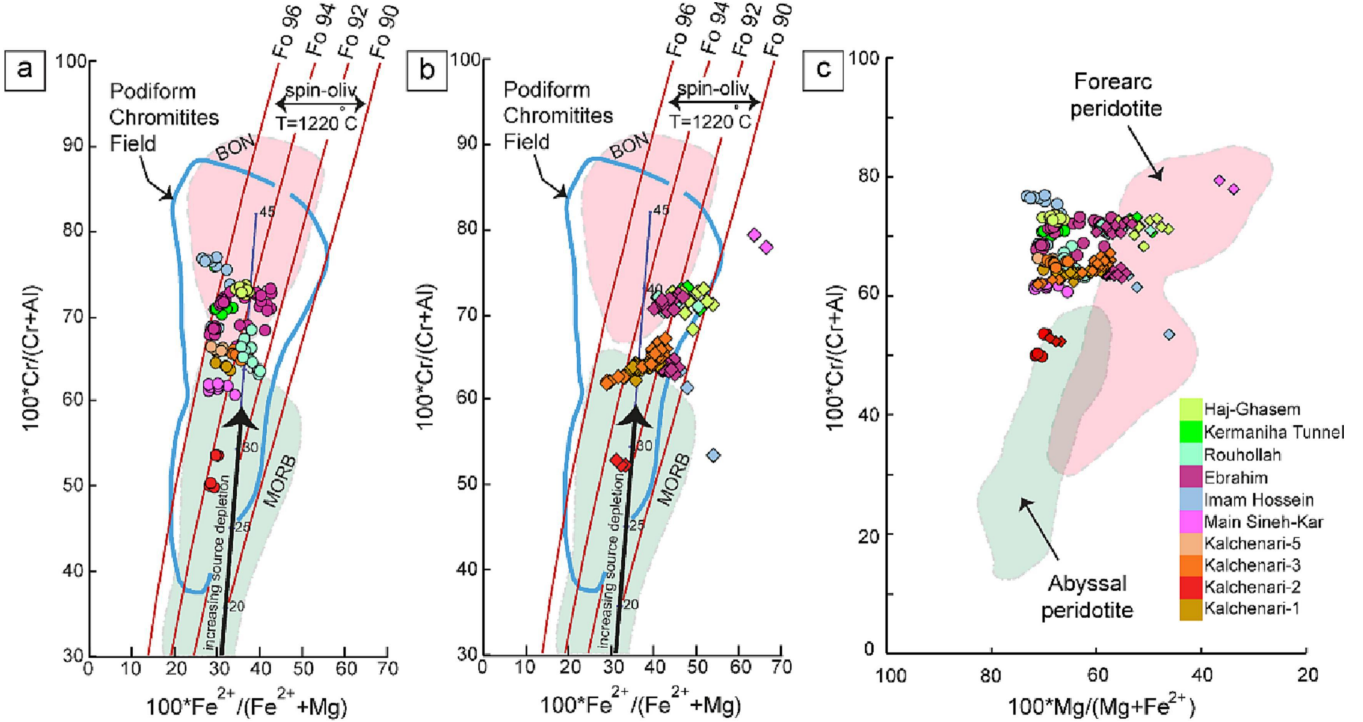
a
b
c
Podiform Chromitites Field
BON
MORB
spin-oliv
T=1220 C
Fo 96
Fo 94
Fo 92
Fo 90
45
40
30
25
20
increasing source depletion
100*Cr/(Cr+Al)
100*Fe2+/(Fe2++Mg)
Forearc peridotite
Abyssal peridotite
100*Mg/(Mg+Fe2+)
Haj-Ghasem
Kermaniha Tunnel
Rouhollah
Ebrahim
Imam Hossein
Main Sineh-Kar
Kalchenari-5
Kalchenari-3
Kalchenari-2
Kalchenari-1

Figure 9

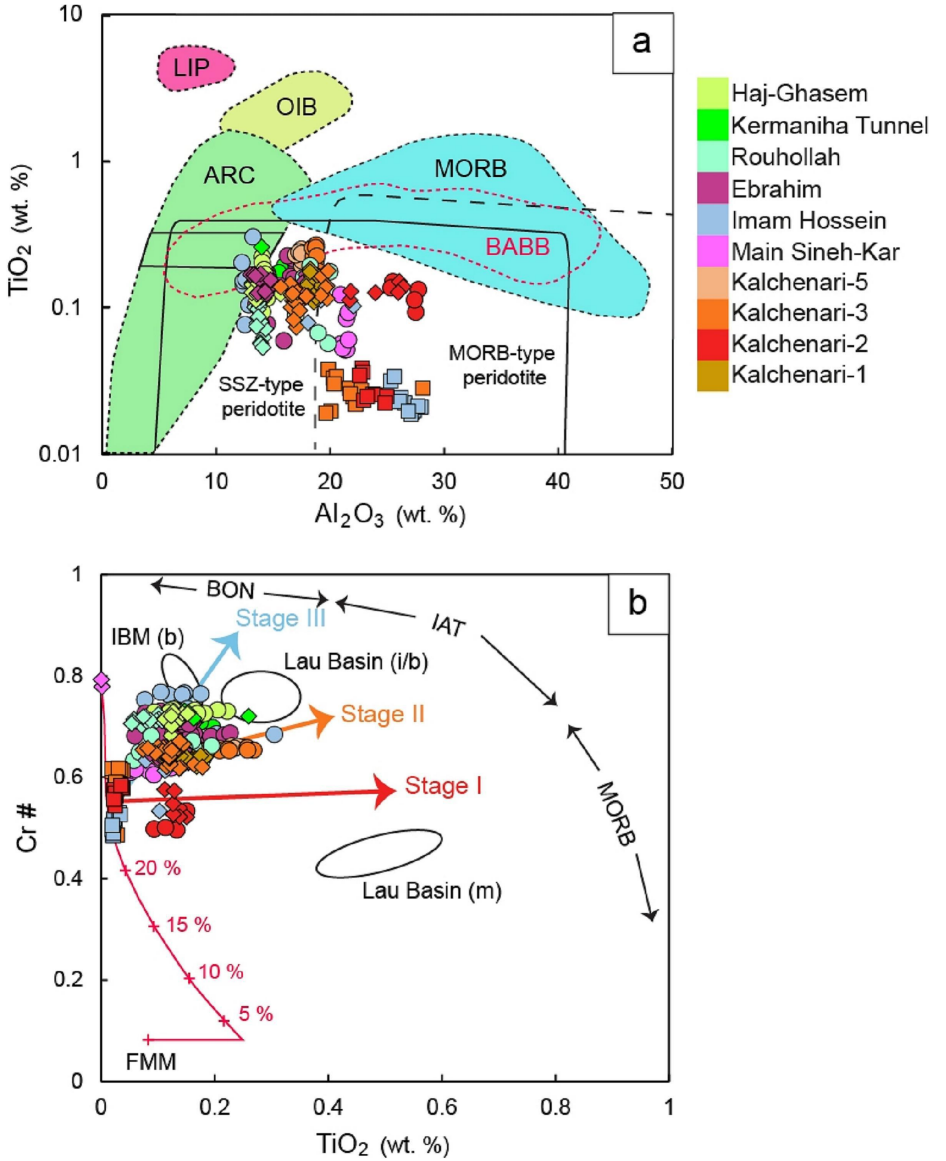
a
LIP
OIB
ARC
MORB
BABB
SSZ-type peridotite
MORB-type peridotite
TiO2 (wt. %)
Al2O3 (wt. %)
10
1
0.1
0.01
0
10
20
30
40
50
Haj-Ghasem
Kermaniha Tunnel
Rouhollah
Ebrahim
Imam Hossein
Main Sineh-Kar
Kalchenari-5
Kalchenari-3
Kalchenari-2
Kalchenari-1
b
BON
IAT
MORB
Stage III
Stage II
Stage I
IBM (b)
Lau Basin (i/b)
Lau Basin (m)
20 %
15 %
10 %
5 %
FMM
Cr #
TiO2 (wt. %)
0
0.2
0.4
0.6
0.8
1

Figure 10

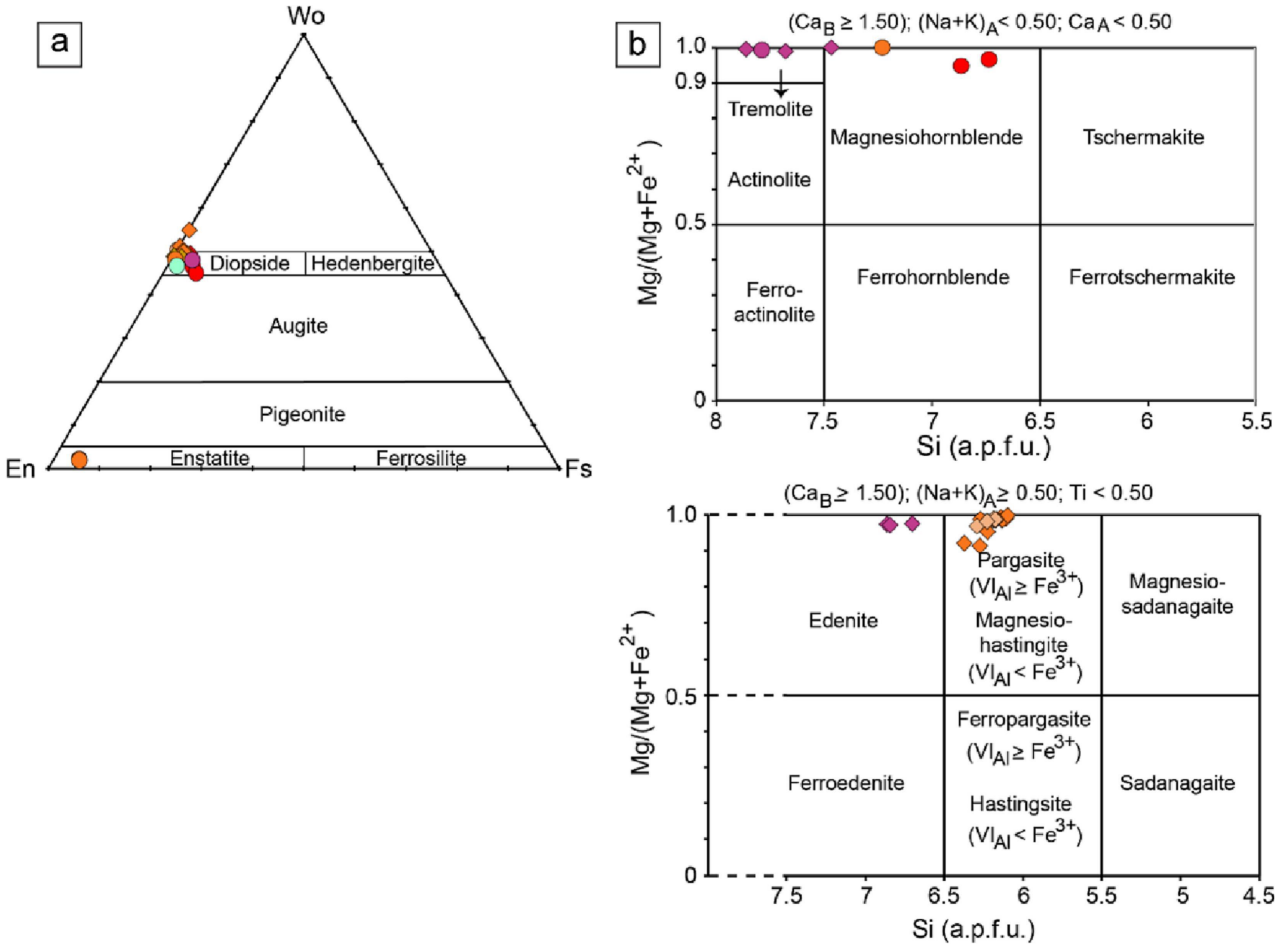
a
Wo
Diopside
Hedenbergite
Augite
Pigeonite
Enstatite
Ferrosilite
En
Fs
b
(Ca_B ≥ 1.50); (Na+K)_A< 0.50; Ca_A < 0.50
Tremolite
Actinolite
Magnesiohornblende
Tschermakite
Ferro-
actinolite
Ferrohornblende
Ferrotschermakite
Mg/(Mg+Fe2+)
Si (a.p.f.u.)
(Ca_B≥ 1.50); (Na+K)_A≥ 0.50; Ti < 0.50
Edenite
Pargasite
(VIAl≥ Fe3+)
Magnesio-
hastingite
(VIAl< Fe3+)
Magnesio-
sadanagaite
Ferropargasite
(VIAl≥ Fe3+)
Ferroedenite
Hastingsite
(VIAl< Fe3+)
Sadanagaite
Mg/(Mg+Fe2+)
Si (a.p.f.u.)

Figure 11

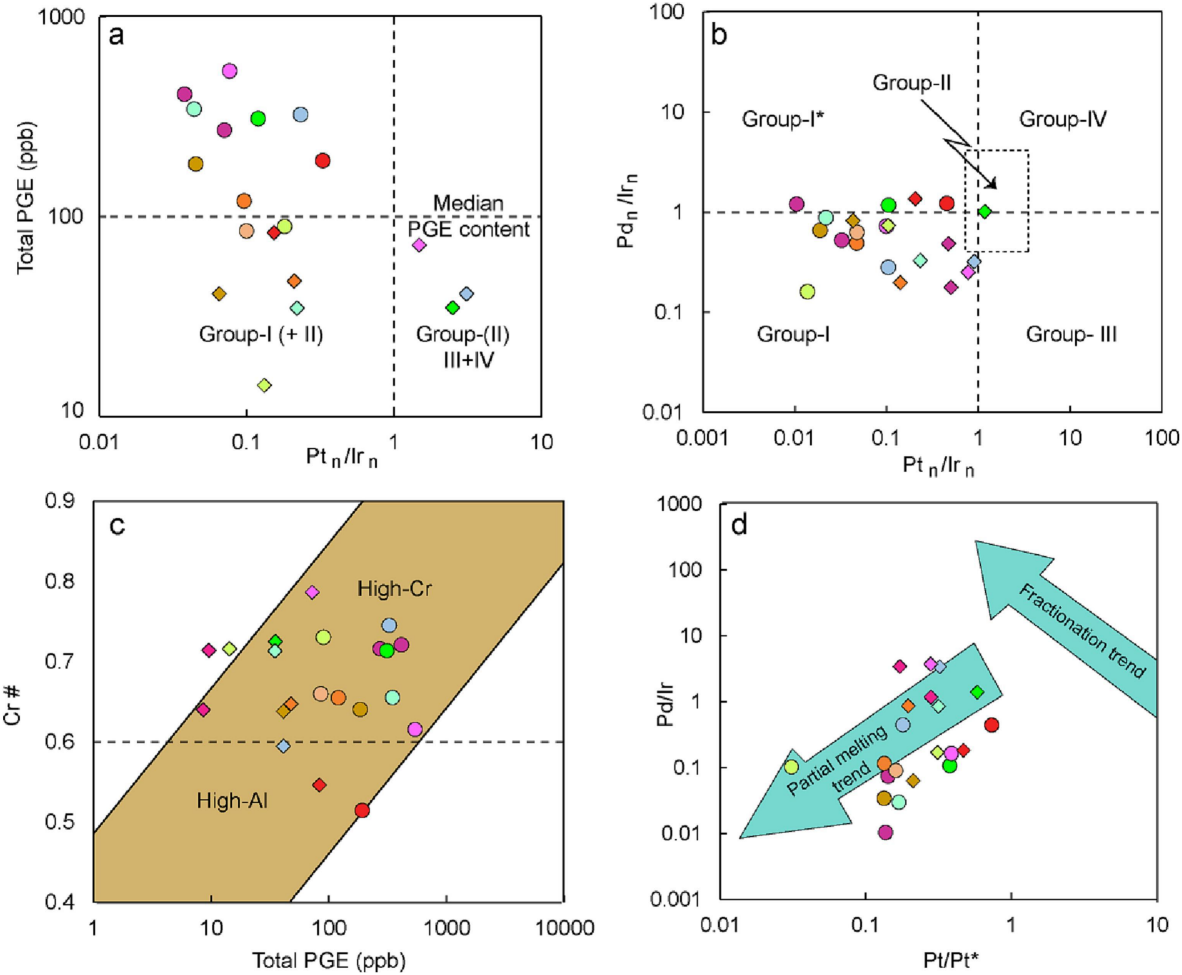
a
Total PGE (ppb)
1000
100
10
0.01
0.1
1
10
Pt n/Ir n
Median
PGE content
Group-I (+ II)
Group-(II)
III+IV
b
100
10
1
0.1
0.01
0.001
0.01
0.1
1
10
100
Pd n /Ir n
Pt n/Ir n
Group-II
Group-I*
Group-IV
Group-I
Group- III
c
Cr #
0.9
0.8
0.7
0.6
0.5
0.4
1
10
100
1000
10000
Total PGE (ppb)
High-Cr
High-Al
d
1000
100
10
1
0.1
0.01
0.001
0.01
0.1
1
10
Pd/Ir
Pt/Pt*
Fractionation trend
Partial melting
trend

Figure 12

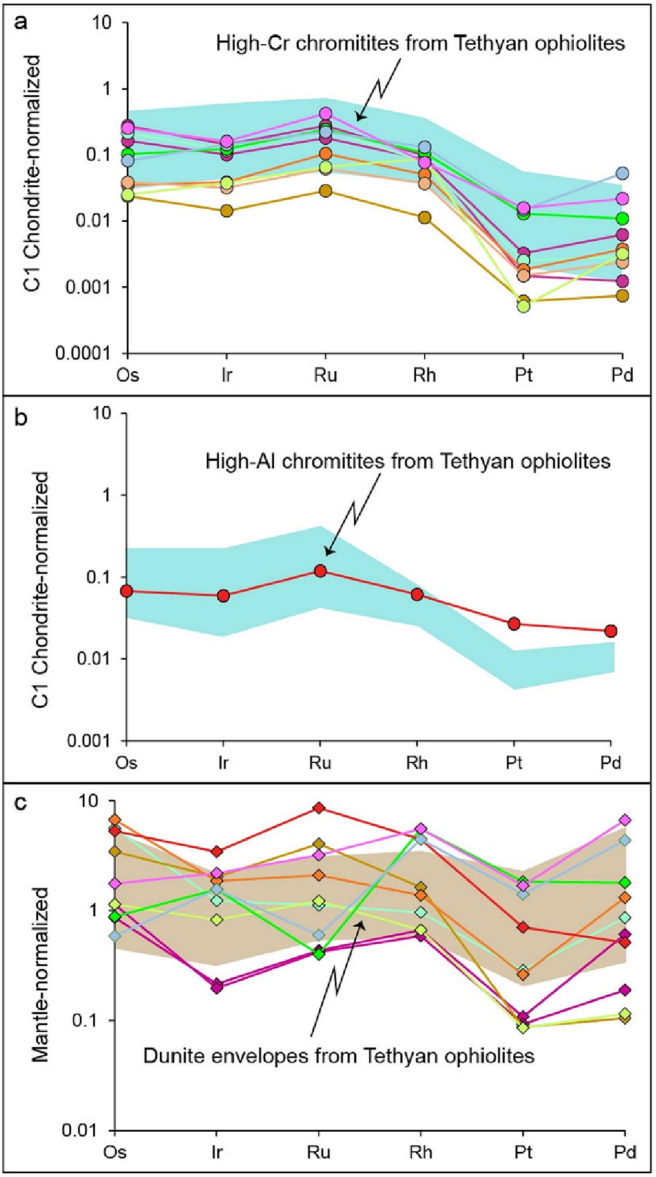
a
High-Cr chromitites from Tethyan ophiolites
C1 Chondrite-normalized
10
1
0.1
0.01
0.001
0.0001
Os
Ir
Ru
Rh
Pt
Pd
b
High-Al chromitites from Tethyan ophiolites
C1 Chondrite-normalized
10
1
0.1
0.01
0.001
Os
Ir
Ru
Rh
Pt
Pd
c
Mantle-normalized
10
1
0.1
0.01
Dunite envelopes from Tethyan ophiolites
Os
Ir
Ru
Rh
Pt
Pd

Figure 13

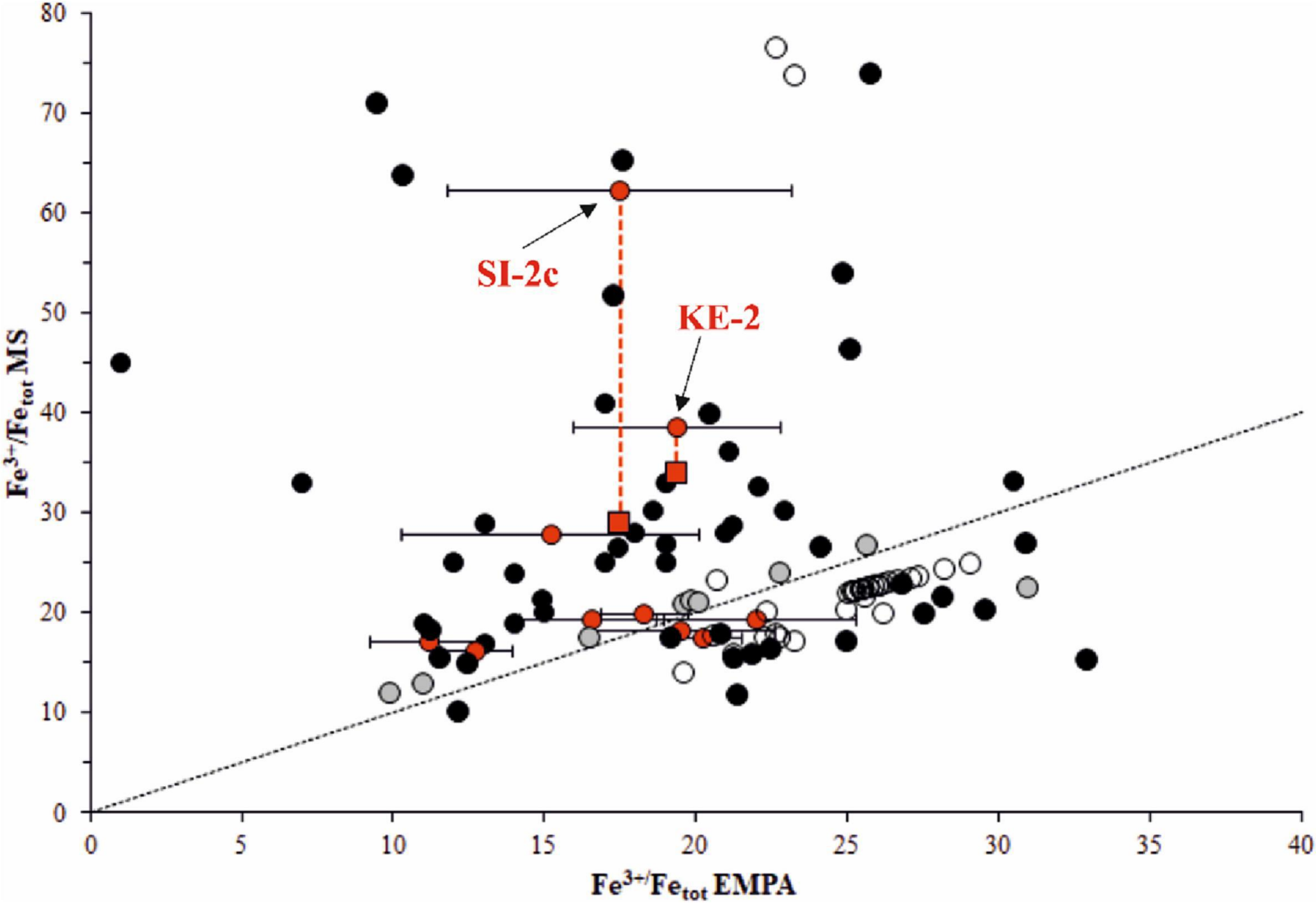
SI-2c
KE-2
Fe^{3+}/Fe_{tot} MS
$Fe^{3+/}Fe_{tot}$ EMPA
0
10
20
30
40
50
60
70
80
0
5
10
15
20
25
30
35
40

Figure 14

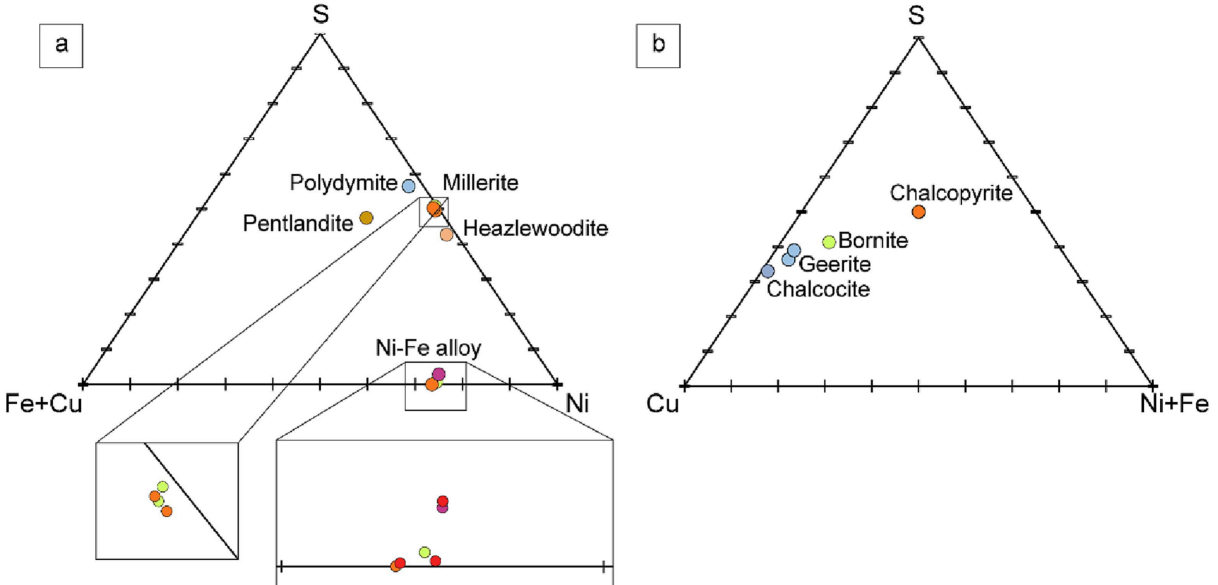
a
S
Polydymite
Millerite
Pentlandite
Heazlewoodite
Ni-Fe alloy
Fe+Cu
Ni
b
S
Chalcopyrite
Bornite
Geerite
Chalcocite
Cu
Ni+Fe

Figure 15

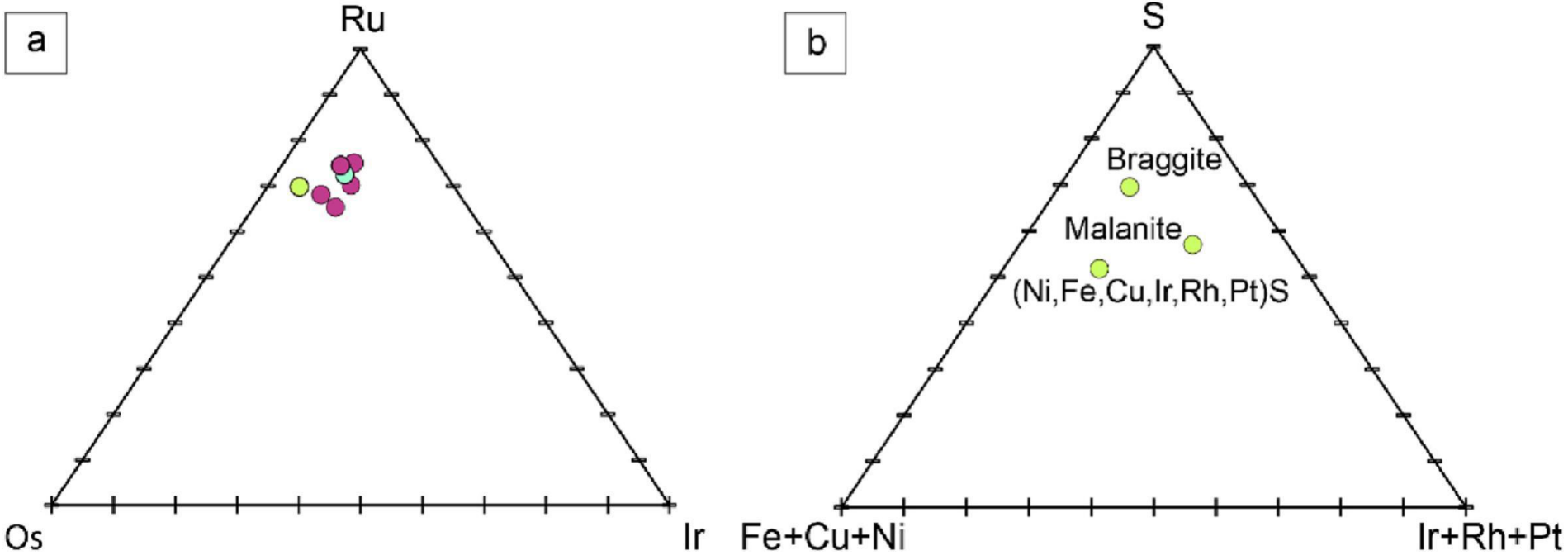
a
Ru
Os
Ir
b
S
Braggite
Malanite
(Ni,Fe,Cu,Ir,Rh,Pt)S
Fe+Cu+Ni
Ir+Rh+Pt

Figure 16

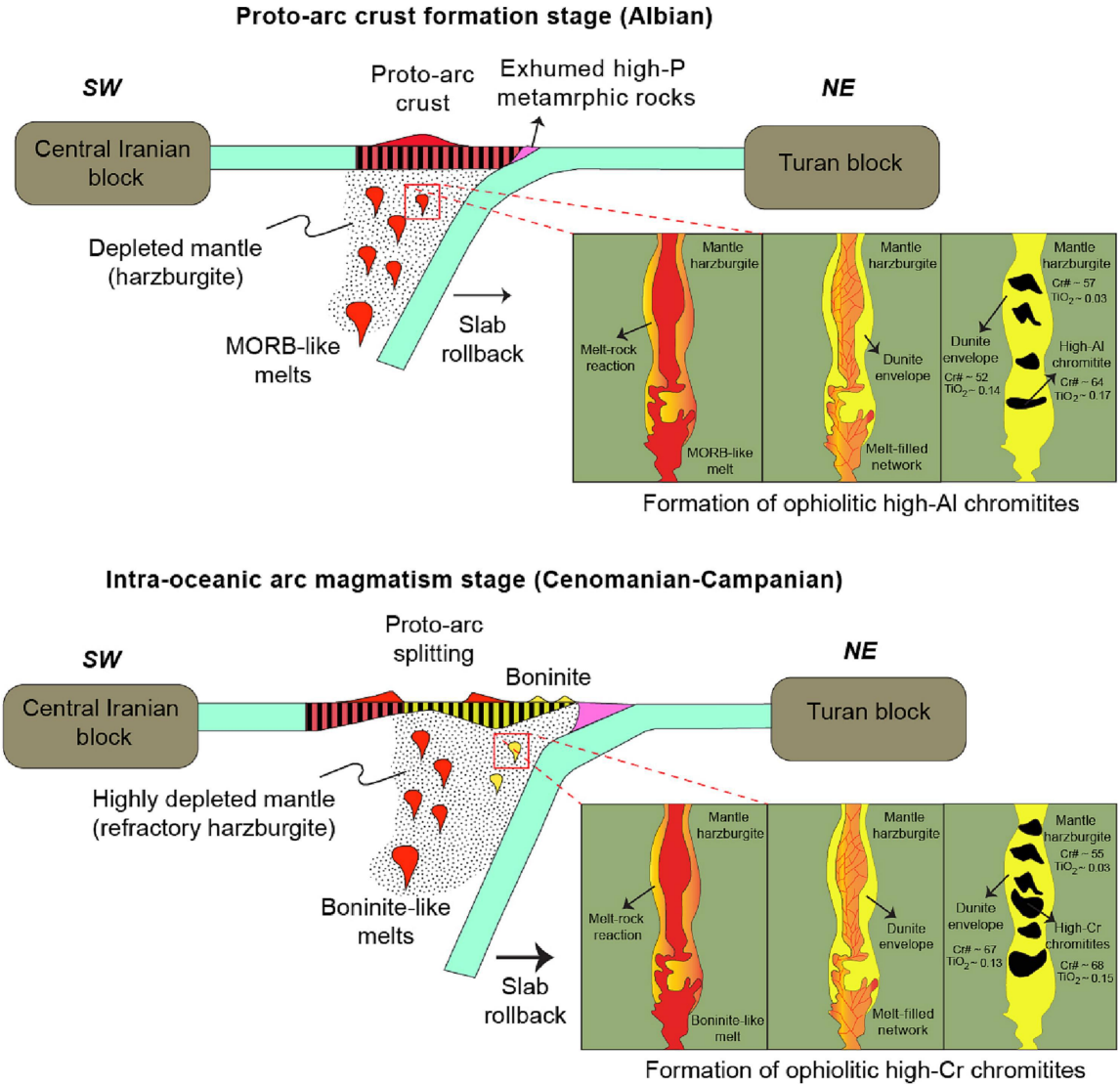
Proto-arc crust formation stage (Albian)
SW
Proto-arc crust
Exhumed high-P metamrphic rocks
NE
Central Iranian block
Turan block
Depleted mantle (harzburgite)
MORB-like melts
Slab rollback
Mantle harzburgite
Melt-rock reaction
MORB-like melt
Mantle harzburgite
Dunite envelope
Melt-filled network
Mantle harzburgite
Cr# ~ 57
TiO2 ~ 0.03
Dunite envelope
Cr# ~ 52
TiO2 ~ 0.14
High-Al chromitite
Cr# ~ 64
TiO2 ~ 0.17
Formation of ophiolitic high-Al chromitites
Intra-oceanic arc magmatism stage (Cenomanian-Campanian)
SW
Proto-arc splitting
Boninite
NE
Central Iranian block
Turan block
Highly depleted mantle (refractory harzburgite)
Boninite-like melts
Slab rollback
Mantle harzburgite
Melt-rock reaction
Boninite-like melt
Mantle harzburgite
Dunite envelope
Melt-filled network
Mantle harzburgite
Cr# ~ 55
TiO2 ~ 0.03
Dunite envelope
Cr# ~ 67
TiO2 ~ 0.13
High-Cr chromitites
Cr# ~ 68
TiO2 ~ 0.15
Formation of ophiolitic high-Cr chromitites

Figure 17